The Astronomical Journal, 169:103 (17pp), 2025 February https://doi.org/10.3847/1538-3881/ada4a4

Excess Ultraviolet Emission at High Galactic Latitudes: A New Horizons View

Jayant Murthy[1], J. Michael Shull[2,3], Marc Postman[4], Joel Wm. Parker[5], Seth Redfield[6], Nathaniel Cunningham[7], G. Randall Gladstone[8,9], Jon P. Pineau[10], Pontus Brandt[11], Anne J. Verbiscer[12], Kelsi N. Singer[5], Harold A. Weaver[11], Richard C. Henry[13], and S. Alan Stern[14]
[1] Indian Institute of Astrophysics, Bengaluru 560 034, India
[2] Department of Astrophysical & Planetary Sciences, CASA, University of Colorado, Boulder, CO 80309, USA
[3] Department of Physics & Astronomy, University of North Carolina, Chapel Hill, NC 27599, USA
[4] Space Telescope Science Institute, 3700 San Martin Drive, Baltimore, MD 21218, USA
[5] Department of Space Studies, Southwest Research Institute, 1301 Walnut Street, Suite 300, Boulder, CO 80302, USA
[6] Astronomy Department and Van Vleck Observatory, Wesleyan University, Middletown, CT 06459, USA
[7] Nebraska Wesleyan University, Lincoln, NE, USA
[8] Southwest Research Institute, San Antonio, TX 78238, USA
[9] University of Texas at San Antonio, San Antonio, TX 78249, USA
[10] Stellar Solutions, Aurora, CO 80011, USA
[11] The Johns Hopkins University Applied Physics Laboratory, Laurel, MD 20723-6099, USA
[12] Department of Astronomy, University of Virginia, Charlottesville, VA 22904, USA
[13] Johns Hopkins University, Department of Physics and Astronomy, Baltimore, 21218, USA
[14] Southwest Research Institute, Space Sector, 1301 Walnut Street, Suite 300, Boulder, CO 80302, USA
Received 2024 November 6; revised 2024 December 25; accepted 2024 December 29; published 2025 January 30

Abstract

We present new observations of the cosmic ultraviolet background (CUVB) at high Galactic latitudes ($|b| > 40°$), made using the Alice UV spectrograph on board the New Horizons spacecraft. These observations were taken at about 57 au from the Sun, outside much of the foreground emission affecting previous missions, and allowed a new determination of the spectrum of the CUVB between 912–1100 Å and 1400–1800 Å. We found a linear correlation between the CUVB and the Planck $E(B-V)$ with offsets at zero-reddening of 221 ± 11 photon units at 1000 Å and 264 ± 24 photon units at 1500 Å (4.4 ± 0.2 nW m^{-2} sr^{-1} at 1000 Å and 5.3 ± 0.5 nW m^{-2} sr^{-1} at 1500 Å). The former is the first firm detection of the offset in the range 912–1100 Å while the latter result confirms previous results from the Galaxy Evolution Explorer, showing that there is little emission from the solar system from 1400 to 1800 Å. About half of the offset may be explained by known sources (the integrated light of unresolved galaxies, unresolved stars, emission from ionized gas, and two-photon emission from warm hydrogen in the halo) with the source of the remaining emission as yet unidentified. There is no detectable emission below the Lyman limit with an upper limit of 3.2 ± 3.0 photon units.

Unified Astronomy Thesaurus concepts: Extrasolar radiation (510); Ultraviolet astronomy (1736); Ultraviolet sources (1741); Ultraviolet spectroscopy (2284); Cosmic background radiation (317); Diffuse radiation (383)

Materials only available in the online version of record: data behind figure

1. Introduction

Measurements of electromagnetic radiation backgrounds are historically important in astrophysics as constraints on the amounts of thermal energy in the microwave background, hot gas in the interstellar medium (ISM), and radiant energy produced by stars, galaxies, and black holes throughout cosmic history. The cosmic microwave background radiation (CMB) discovered in 1965 (A. A. Penzias & R. W. Wilson 1965; R. H. Dicke et al. 1965) solidified the "hot Big Bang" model and led to many future applications in precision cosmology (P. J. E. Peebles 2020). Observations of thermal anisotropies in the CMB are critical for deriving fundamental cosmological parameters from the Wilkinson Microwave Anisotropy Probe (C. L. Bennett et al. 2003; D. N. Spergel et al. 2003) and the Planck satellite (Planck Collaboration et al. 2014; Planck Collaboration VI 2020).

An isotropic X-ray (2–10 keV) background, first detected in rocket observations (R. Giacconi et al. 1962), was initially interpreted as evidence for a hot intergalactic medium with significant baryon content. Subsequent X-ray imaging from large satellites (HEAO, ROSAT, Einstein Observatory) found a more complex situation, employing higher spatial resolution and spectra over a wide energy range (see X. Barcons & A. C. Fabian 1992 for a review). These improved observations showed that the X-ray background comes from resolved nonthermal Galactic and extragalactic sources and diffuse soft X-ray emission from local hot interstellar gas. At high Galactic latitudes, a significant fraction of the diffuse background at 1 keV can be resolved into discrete sources. However, in the 0.1–0.3 keV band, the photon mean free path is limited to less than 100 pc at mean hydrogen density $n_{\rm H} \approx 1$ cm^{-3}. Within the Local Bubble, which extends 60–100 pc from the Sun (R. Lallement et al. 2003) and is comprised of hot (10^6 K), low density ($n_{\rm H} \approx 0.01$ cm^{-3}) gas, the mean free path will be longer (C. L. Snowden et al. 1990; P. C. Frisch et al. 2011). While there is a 0.1–0.3 keV contribution from charge exchange within the heliosphere (T. E. Cravens 2000; R. Lallement 2004), a significant fraction of soft X-rays is coming from the hot Local Bubble gas (M. Galeazzi et al. 2014).

This cosmic optical background (COB) has been the topic of several recent studies (S. P. Driver et al. 2016; K. Mattila et al. 2017; A. Saldana-Lopez et al. 2021) which have included deep

images (M. Zemcov et al. 2017; T. R. Lauer et al. 2021, 2022; T. Symons et al. 2023; M. Postman et al. 2024) taken with LORRI, the Long-Range Reconnaissance Imager (A. F. Cheng et al. 2008; H. A. Weaver et al. 2020) on board NASA's New Horizons (NH) spacecraft. This background measures the redshifted radiation produced by stars and gas in galaxies over the history of the Universe and serves as an important test of cosmological star formation models. M. Postman et al. (2024) used multiple LORRI images taken from far beyond zodiacal light interference in the distant Kuiper Belt to measure the COB integrated from 0.4 to 0.9 μm. That survey included 16 fields at high Galactic latitudes, selected to minimize scattered light from the Milky Way galaxy. These were augmented by eight calibration fields for diffuse Galactic light (DGL) and several auxiliary fields. The survey is free of the zodiacal light produced by sunlight scattered by interplanetary dust and supersedes an earlier analysis (T. R. Lauer et al. 2022) based on observations of one of the present fields. Isolating the COB contribution to the raw total sky levels measured in the fields required subtracting the remaining scattered light from bright stars and galaxies, the intensity from stars within the fields fainter than the photometric detection limit, and the DGL foreground. The LORRI survey yielded a highly significant detection (6.7σ) of the COB at 11.08 ± 1.65 nW m^{-2} sr^{-1} at the pivot wavelength of 0.608 μm. The estimated integrated intensity from background galaxies, 8.17 ± 1.18 nW m^{-2} sr^{-1}, accounts for the majority of this signal and is the most precise measurement of the COB to date.

The current paper describes NH observations of the cosmic ultraviolet background (CUVB) radiation taken in parallel with the LORRI observations, but with small pointing offsets. The data were taken in the far-ultraviolet (FUV) by the Alice spectrograph (S. A. Stern et al. 2008) on board the New Horizons spacecraft at a distance of 57 au from the Sun, outside most of the interplanetary gas and dust that complicates such observations. Radiation in the FUV band (conventionally from 912 to 2000 Å) is important for studying a variety of astrophysical processes: massive star formation and ionized gas in the Galactic ISM; heating of diffuse interstellar gas clouds by photoelectric emission from dust; controlling the interstellar atomic-to-molecular transition through photodissociation in the H2 Lyman and Werner bands; and the star formation rate in galaxies over billions of years.

Measurements of the CUVB surface brightness have a long history with a variety of instruments (see reviews by S. Bowyer 1991; R. C. Henry 1991; J. Murthy 2009). These studies began with observations from sounding rockets (S. Hayakawa et al. 1969; R. C. Henry et al. 1977; R. C. Anderson et al. 1979; P. D. Tennyson et al. 1988) and continued with space-borne experiments on board OAO-2 (C. F. Lillie & A. N. Witt 1976), Apollo 17 (R. C. Henry et al. 1978), Voyager (J. Murthy et al. 1999; J. Murthy et al. 2012), and the Galaxy Evolution Explorer (GALEX; J. Murthy et al. 2010; E. T. Hamden et al. 2013; M. S. Akshaya et al. 2018, 2019; Y.-K. Chiang et al. 2019). The CUVB has been found to be correlated with the amount of dust in the line of sight, usually represented by the color excess $E(B-V)$. Although this relationship saturates at low Galactic latitudes where the optical depth of the interstellar dust is high, there is a linear correlation of the CUVB and the $E(B-V)$ at high Galactic latitudes where the optical depth of the dust is less than 1 (J. Murthy 2016). This part of the CUVB is due to the scattering of starlight from hot stars in the Galactic Plane by the interstellar dust in the line of sight (M. Jura 1979). The offsets, after subtraction of the dust-scattered light, represent any other isotropic emission, such as line emission from halo gas, the integrated light from unresolved galaxies, and other Galactic and extragalactic sources.

Table 1
Observations of the CUVB Offset at the Poles

Reference	Wavelength (Å)	Offset[a]	Instrument
R. C. Henry et al. (1978)	1180–1680	250	Apollo 17
R. C. Anderson et al. (1979)	1230–1680	285 ± 32	Rocket
F. Paresce et al. (1980)	1350–1550	<300	ASTP
P. D. Feldman et al. (1981)	1200–1670	150 ± 50	Rocket
M. Joubert et al. (1983)	1690	300–690	D2B
P. Jakobsen et al. (1984)	1590	<550	Rocket
	1710	<900	
J. B. Holberg (1986)	900–1100	<200	Voyager
T. Onaka & K. Kodaira (1991)	1500	200–300	Rocket
R. C. Henry & J. Murthy (1993)	1500	300 ± 100	UVX
A. N. Witt & J. K. Petersohn (1994)	1500	300 ± 80	DE-1
A. N. Witt et al. (1997)	1400–1800	160 ± 50	FAUST
D. Schiminovich et al. (2001)	1740	200 ± 100	NUVIEWS
E. T. Hamden et al. (2013)	1565	300	GALEX
M. S. Akshaya et al. (2018)	1565	240–290	GALEX
M. S. Akshaya et al. (2019)	1565	240 ± 18	GALEX

Note.
[a] The offset is the remaining emission after subtraction of the dust-scattered light in photon units (ph cm^{-2} s^{-1} sr^{-1} Å^{-1}).

There have been many observations of the CUVB near the Galactic Poles, finding offsets of 230–290 ph cm^{-2} s^{-1} sr^{-1} Å^{-1} (Table 1). These units are commonly referred to as "photon units" or "continuum units." In the literature, integrated backgrounds are often converted to monochromatic fluxes, $\nu I_\nu = \lambda I_\lambda$ in nW m^{-2} sr^{-1}, with the usual relation between flux distributions. Defining photon flux $\Phi_\lambda = I_\lambda/h\nu = (\lambda I_\lambda/hc)$ at the central wavelength of the FUV band and taking care with Å-to-cm conversion in the units, we find that 300 photon units = 5.96 nW m^{-2} sr^{-1}. The integral of photon flux times energy (hc/λ) over the wavelength band can be expressed

$$\int_{\lambda_1}^{\lambda_2} \frac{hc}{\lambda}\,\Phi_\lambda\,d\lambda \approx hc\;\bar{\Phi}_\lambda \ln(\lambda_2/\lambda_1) = \langle \lambda I_\lambda \rangle \ln(\lambda_2/\lambda_1)\;, \quad (1)$$

where $\bar{\Phi}_\lambda$ and $\langle \lambda I_\lambda \rangle$ are evaluated at band center. By convention, most background surveys quote λI_λ without the factor $\ln(\lambda_2/\lambda_1)$, an approximation that overestimates the actual width of the FUV band of GALEX (440 Å at $\lambda_{\rm eff} \approx 1530$ Å).

The observed values of the offsets (Table 1) are considerably greater than the 73 ± 16 photon units expected from galaxy counts (S. P. Driver et al. 2016), with other suggested examples of possible FUV sources, including the two-photon continuum produced from H I ($2s \rightarrow 1s$) emission produced in the warm ionized interstellar medium and low-velocity shocks (R. J. Reynolds 1992; S. R. Kulkarni 2022; S. R. Kulkarni & J. M. Shull 2023), and the radiative decay of massive neutrinos (D. W. Sciama 1990) or other dark matter (J. A. Kollmeier et al. 2014; R. C. Henry et al. 2015). S. R. Kulkarni (2022) suggested that much (41–60 photon units) of the excess emission of 80–230 photon units was due to two-photon emission arising in the Earth's atmosphere or in the

interplanetary medium, as the earlier observations were generally made from low Earth orbit. We note that instrumental scattered light from off-axis stars may contribute to the observed signal, but this will be minimized at the Galactic poles where there are few bright UV stars.

The spectral region between 912 and 1200 Å is much more difficult to observe because of internal scattering from the Lyα line, either from the Earth's atmosphere or from the interplanetary medium. There has been only one observation at the Galactic poles using the Voyager ultraviolet spectrometers (UVS), which was only able to set an upper limit of about 200 photon units on the observed CUVB from 912 to 1150 Å (J. B. Holberg 1986). Although the two Voyager UVS were able to detect the diffuse UV background in many parts of the sky, these observations were at the limit of the instrument's capabilities and could not significantly constrain the extragalactic background light (EBL) below 1200 Å, especially because of the uncertain contribution due to internal scattering of interplanetary Lyα.

The NH CUVB program was designed to measure the diffuse UV radiation field as viewed from the Kuiper Belt at a distance of 57 au from the Sun, beyond the bulk of the emission from the solar system. We will describe the analysis of the New Horizons Alice data and will discuss the measurement of the offsets. Those observations in the 1400–1800 Å band are consistent with earlier observations made from Earth orbit. Our determination of the offsets between 912 and 1150 Å is the first such in this band and is possible only because of the much lower contributions of the interplanetary hydrogen lines at this distance from the Sun.

2. The CUVB Survey

2.1. The New Horizons Alice UV Spectrograph

The New Horizons Alice spectrograph (S. A. Stern 2008) is a Rowland Circle spectrograph with spectral coverage from 520 to 1870 Å, enabling direct measurement of the FUV cosmic background over these wavelengths. The main airglow channel (AGC) has an aperture comprising two connected areas on the sky: a narrow "Stem" with a field of view (FOV) of $0.^{\circ}1 \times 4.^{\circ}0$ and a square "Box" with an FOV of $2.^{\circ}0 \times 2.^{\circ}0$ (Figure 1). The full detector image is 1024 pixels in the spectral direction and 32 pixels in the spatial direction. The full slit illuminates roughly rows 6–25 (zero-indexed) on the detector data array, with the Stem portion of the slit illuminating rows 6–18 and the Box portion illuminating rows 19–25, with row 18 serving as a transition between the two slit widths. Row 16 defines the instrument boresight. The full width at half-maximum (FWHM) spectral resolution for point sources for the Stem and the Box is 1–3 Å and 5 Å, respectively, and spatially each row is 0.3 deg along the slit. The Alice detector is an intensified Z-stack microchannel plate (MCP) with a split coating of KBr (520–1180 Å) and CsI (1250–1870 Å) to cover the entire spectral range. The MCP was masked around the Lyα line (1216 Å) during the coating process to reduce sensitivity to that intense interplanetary line. The Lyα line is approximately in the center of the spectral range with an FWHM (for aperture-filling diffuse sources) of 9 ± 1.4 Å for the Stem and 172 Å for the Box (S. A. Stern et al. 2008). For the present survey, no CUVB measurements include detector regions directly illuminated by Lyα; however, as we will show, much of the observed signal is from dark counts and

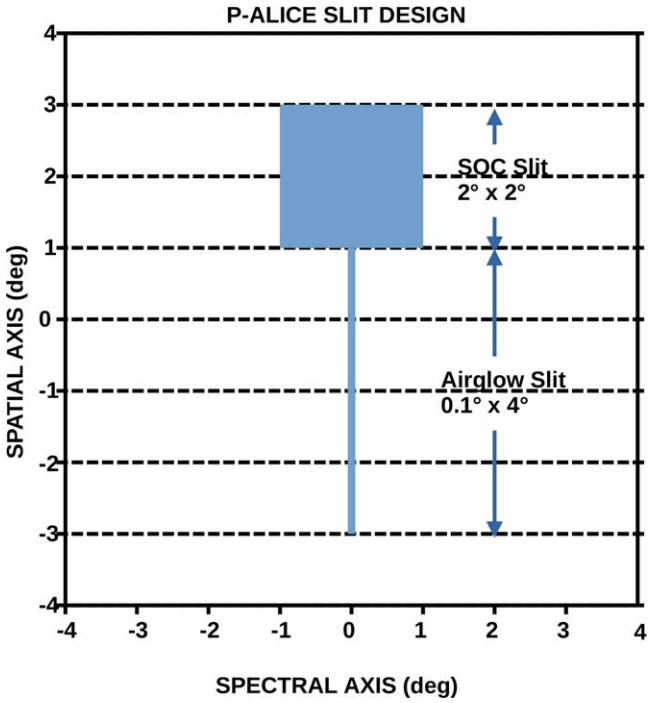

Figure 1. The Alice entrance aperture is a square Box on top of a narrow, rectangular Stem (S. A. Stern 2008).

instrumental scattering of the intense Lyα line, which have to be modeled and subtracted from the data.

The AGC has a controllable aperture door which, when closed, permits an accurate measurement of the detector's dark current. We will detail the strategy for accurate measurement of the dark signal, which represents a significant fraction of the raw total signal of the on-sky observations, in Section 2.3. In this context, we also note that Alice has a special solar occultation channel (SOCC), which enabled observation of UV transmission spectra of Pluto's atmosphere. The SOCC is mounted at a 90° angle to the AGC boresight and has an optical path to the detector that is not shuttered. As it is intended for observation of the Sun, its throughput is a factor of 6400 less than the AGC, but it does represent a light leak into the instrument from the sky. As we detail in Section 2.2, the spacecraft was oriented during the CUVB observations to place the SOCC port within the spacecraft shadow (see Figure 2).

2.2. The Survey Design and Field Selection

The CUVB survey was designed in parallel with the NH COB survey, described by M. Postman et al. (2024). In brief, they observed several fields with the New Horizons LORRI instrument to measure the COB intensity and calibrate the observations. Of these, 16 fields were selected for primary observation of the COB intensity; these were designated with the "NCOB" prefix. Eight additional fields, designated with the "DCAL" prefix, were selected to develop a DGL estimator when used in league with the NCOB fields. Each of the LORRI NCOB and DCAL fields has a corresponding Alice field in the present survey to measure the CUVB intensity, albeit with small positional differences, as we detail below. The CUVB program also includes four additional fields unique to the CUVB program for calibration purposes.

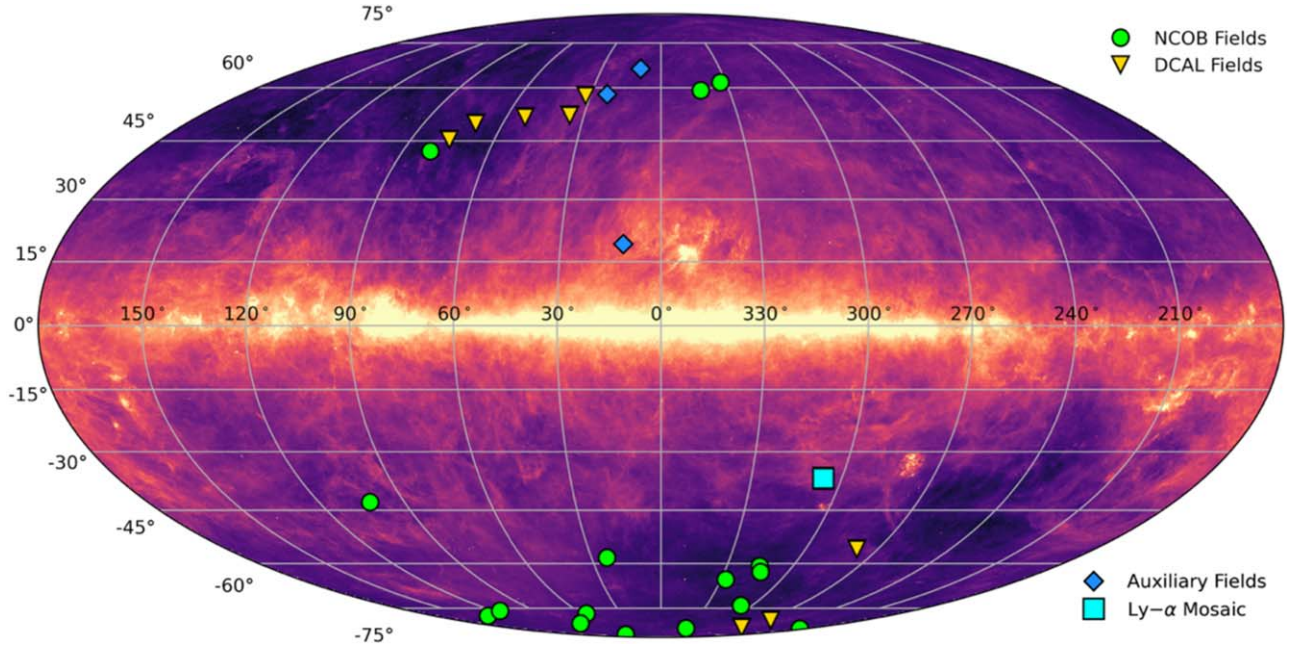

Figure 2. The locations of the CUVB fields are shown on the Infrared Interferometer in Space (Improved Reprocessing of the *IRAS* Survey) full-sky 100 μm map (M. A. Miville-Deschênes & G. Lagache 2005) in Galactic coordinates. The auxiliary fields include the two shock fields and one molecular hydrogen field.

The overall geometry of the COB and CUVB surveys was specified by the trajectory of NH out of the solar system, the requirement that the Alice and LORRI apertures be positioned in the spacecraft shadow to avoid scattered sunlight affecting the background measurements, and avoidance of the dense regions of the Milky Way plane. The spacecraft trajectory in turn was specified by NH's primary mission of obtaining the first exploration of Pluto (S. A. Stern et al. 2015) and then the Kuiper Belt object Arrokoth (S. A. Stern et al. 2019).

During the NH mission, Pluto, as seen from the Earth, was projected against the bulge of the Milky Way. This means that the "antisolar" hemisphere suitable for background measurements is roughly centered on the heart of our Galaxy. In detail, we selected fields with solar elongation angle (SEA) $> 95°$. While SEA $> 90°$ would be sufficient to keep direct sunlight out of the instrument apertures, the spacecraft bulkhead in which the apertures are positioned supports other instruments that could potentially scatter sunlight into the apertures; SEA $> 95°$ ensures that these are also shaded by the spacecraft (T. R. Lauer et al. 2021). Fields were selected with Galactic latitude $|b| > 40°$ to avoid dense stellar foregrounds and to minimize the contribution from dust-scattered starlight. Lastly, ecliptic latitudes were restricted to $|\beta| > 15°$. While NH is not directly affected by zodiacal light, the far-infrared (FIR) intensities that were used to select fields for low DGL are provided by maps made in Earth space and thus may incur larger errors near the ecliptic (S. Matsuura et al. 2011; T. Carleton et al. 2022; P. M. Korngut et al. 2022).

The combination of these constraints left 4239 deg^2 of sky available. M. Postman et al. (2024) randomly selected 60,000 positions within this area, and estimated the DGL contribution for each one using the Infrared Interferometer in Space (IRIS) 100 μm all-sky data (M. A. Miville-Deschênes & G. Lagache 2005).[15] The 16 NCOB fields were selected to minimize estimated DGL and provide good angular coverage around the sky. The fields were also selected to minimize scattered starlight in the LORRI field, although this was not a concern for the present Alice observations because there are so few bright stars in the UV, particularly at high Galactic latitudes.

The eight DCAL fields were selected to perform an improved self-calibration of the relation of FIR intensity to UV DGL in combination with the NCOB fields. As such, they were located to cover fields with progressively higher 100μm surface brightness, up to a limit of ~3 MJy sr^{-1}. This limit was selected to avoid dust optical depths large enough that nonlinear behavior between the FIR intensity and scattered light amplitude might occur.

The final coordinates of each Alice NCOB and DCAL field were adjusted by up to ~1.°5 compared to the corresponding LORRI field to minimize the presence of UV-bright stars within the Alice FOV. The orientation of the fields was also rolled about the Alice optical axis to bring the SOCC aperture within the spacecraft shadow.

Lastly, four fields unique to the CUVB program were defined to improve the calibration of the Alice instrument or to augment the analysis of the observations. Two fields, designated SHOCK1 and SHOCK2, were defined to observe UV emission from highly shocked gas associated with the Fermi/eROSITA bubbles at Galactic latitudes 57.°6 and 65.°4, respectively. H2_NE is a low Galactic latitude field selected to observe possible molecular hydrogen (H_2) fluorescent emission. LYACAL is a reobservation of a mosaic of a contiguous area of Box fields first observed with Alice in 2007 when the spacecraft was ~8 au from the Sun, with the goal of characterizing the Lyα scattering function of the Alice spectrograph (see Section 3.3). Differencing the 2023 and 2007 data sets removes invariant astrophysical sources common to both, isolating the solar Lyα emission, which has decreased as the spacecraft traveled to 57 au (J. Murthy et al. 1999; G. R. Gladstone et al. 2018).

The coordinates, and observation dates for the CUVB fields are listed in Table 2. The mission elapsed time (MET) identifiers of the first observation of each field are also given.

[15] M. Postman et al. (2024) developed an improved DGL estimator based on Planck 350 μm and 550 μm intensities but used the M. Zemcov et al. (2018) DGL estimator at 100 μm for the initial definition of the COB survey.

Table 2
Survey Field Centers and Observations

Field ID	R.A. (J2000) (deg)	Decl. (deg)	UT Date	MET (s)	Stem l (deg)	Stem b (deg)	Box l (deg)	Box b (deg)	Stem $E(B-V)$	Box $E(B-V)$
NHTF01	359.559	−23.654	2021-09-24	0494772718	57.38	−76.40	51.93	−78.98	0.013	0.018
NCOB01	6.415	−56.809	2023-09-13	0556922877	313.30	−61.03	318.88	−60.12	0.017	0.013
NCOB02	8.410	−54.967	2023-08-30	0555729417	313.49	−63.51	312.02	−60.70	0.016	0.016
NCOB03	0.443	−47.405	2023-08-21	0554939877	325.99	−65.55	331.63	−63.94	0.014	0.014
NCOB04	12.983	−41.939	2023-08-20	0554877517	305.36	−74.57	311.98	−72.34	0.012	0.011
NCOB05	8.762	−23.312	2023-08-28	0555543697	84.36	−86.79	116.06	−87.85	0.012	0.013
NCOB06	11.659	−35.055	2023-09-12	0556828417	336.32	−84.42	324.18	−81.82	0.015	0.011
NCOB07	20.604	−24.683	2023-08-27	0555482077	184.71	−83.37	209.75	−84.38	0.018	0.015
NCOB08	334.996	−25.720	2023-08-30	0555667297	24.99	−58.13	19.55	−58.38	0.014	0.011
NCOB09	6.231	−20.811	2023-08-29	0555608978	81.04	−80.57	66.93	−82.49	0.014	0.013
NCOB10	18.288	−16.543	2023-08-27	0555420517	135.27	−77.06	137.93	−79.83	0.015	0.014
NCOB11	9.843	−13.184	2023-08-26	0555358257	115.88	−75.09	114.03	−77.89	0.017	0.013
NCOB12	204.187	2.155	2023-08-17	0554554437	331.73	60.86	334.62	63.38	0.025	0.025
NCOB13	211.930	2.394	2023-08-17	0554547508	341.55	58.37	344.92	60.66	0.030	0.024
NCOB14	356.932	17.336	2023-08-20	0554837698	103.05	−42.59	99.44	−43.73	0.073	0.058
NCOB15	247.924	52.331	2023-08-13	0554209418	79.25	42.35	83.04	41.76	0.025	0.021
DCAL01	20.257	−30.111	2023-08-20	0554845297	260.77	−83.94	276.07	−81.65	0.022	0.018
DCAL02	24.026	−34.454	2023-09-12	0556796457	260.38	−80.80	264.89	−77.99	0.023	0.017
DCAL03	236.278	43.411	2023-08-13	0554247327	69.05	49.90	73.40	49.32	0.020	0.017
DCAL04	240.679	47.617	2023-08-13	0554216007	74.83	45.48	78.83	44.88	0.014	0.026
DCAL05	239.889	35.271	2023-08-14	0554300848	51.12	51.52	55.74	51.58	0.033	0.027
DCAL06	37.452	−56.481	2023-09-13	0556916078	277.65	−56.38	281.09	−54.25	0.041	0.039
DCAL07	228.234	22.238	2023-08-15	0554367758	30.54	57.45	35.77	58.13	0.048	0.053
DCAL08	234.766	22.599	2023-08-14	0554336068	34.12	51.79	38.66	52.46	0.061	0.055
LYACAL	10.095	−35.029	2023-08-22	0555002780	306.70	−35.62	306.35	−38.47	0.160	0.076
H2_NE	257.709	−9.334	2023-09-06	0556334397	10.34	19.53	13.01	18.14	0.747	0.594
SHOCK1	226.189	17.788	2023-08-15	0554428408	21.55	57.64	26.63	58.65	0.032	0.042
SHOCK2	215.952	15.941	2023-08-16	0554488058	8.33	65.37	14.50	66.75	0.020	0.020

Note. The R.A. and decl. values refer to the coordinates of the overall Alice boresight, while Galactic coordinates are given for the centers of the separate Stem and Box apertures. All coordinates are in degrees. MET is the mission elapsed time in seconds (from the launch on 14:00 ET on 2006 January 19) of the first image in each field sequence. NCOB fields are the primary fields for measuring the COB intensity. NHTF01 is the test of the NCOB field selection and observational strategy published initially in T. R. Lauer et al. (2022) and reanalyzed in M. Postman et al. (2024). DCAL fields are for DGL calibration. $E(B-V)$ values are the mean values in the Stem and the Box, respectively, from Planck Collaboration et al. (2016) with a typical variation of 5 mmag.

Figure 2 shows the field distribution on the sky with respect to the IRIS 100 μm map (M. A. Miville-Deschênes & G. Lagache 2005).

2.3. The CUVB Observations

A sequence of individual exposures, using the Alice Histogram Imaging Mode (HIM), was taken at each field. The histogram data consists of FITS (W. D. Pence et al. 2010) images with the counts integrated over the entire observation (Figure 3). The detector image is 1024 pixels in the spectral direction and 32 pixels in the spatial direction, with the extent of the Stem and the Box shown in Figure 1. The Stem spectrum is extracted from rows 6 to 15 (inclusive), and the Box spectrum is extracted from rows 20 to 24 to minimize any vignetting effects near the edge and Stem/Box transition of the slit. The Lyα line is approximately in the center of the spectral range with a full width at half-maximum (FWHM) of 9 Å for the Stem and 172 Å for the Box.

An important consideration for understanding the region of the sky observed in any observation is that the pointing of NH is controlled by monopropellant thrusters rather than the precise reaction wheels used in spacecraft such as the Hubble Space Telescope (HST) or JWST. For Alice observations, the integrations are conducted with a $0.^{\circ}14$ guidance deadband, which means that the Alice aperture will wander around the sky within this distance from the commanded pointing. As this is larger than the width of the Alice stem, this means that the area of the sky at each pointing that it samples is at least twice its width. For precise use, spacecraft telemetry is available, showing the trajectory of the Alice aperture over any observation.

A major concern was the accurate and precise measurement of the Alice dark current, which contributes a significant fraction of the total signal in the sky exposures. To this end, Alice's observations commenced only after a 5 hr thermal stabilization period following the activation of the instrument. This interval was considered adequate to counter the small temperature-dependent variations in Alice sensitivity seen on shorter timescales following power-on.

The standard observing sequence for any field was to start with a 3600 s dark exposure (aperture door closed), followed by several sets of a 3600 s sky and 3600 s dark exposure pairs. This way, the individual sky exposures are always interlaced between dark exposures, allowing any slow drift in the dark current to be tracked. For the NCOB and auxiliary fields, eight individual sky exposures of 3600 s each were obtained for a 28,800 s total exposure, again interlaced between nine dark exposures. For the DCAL fields, four 3600 s sky exposures, for a total of 14,400 s, were interlaced between five dark exposures. The dark observations taken during the Alice mission are listed in Table 3 and will be discussed in Section 3.2.

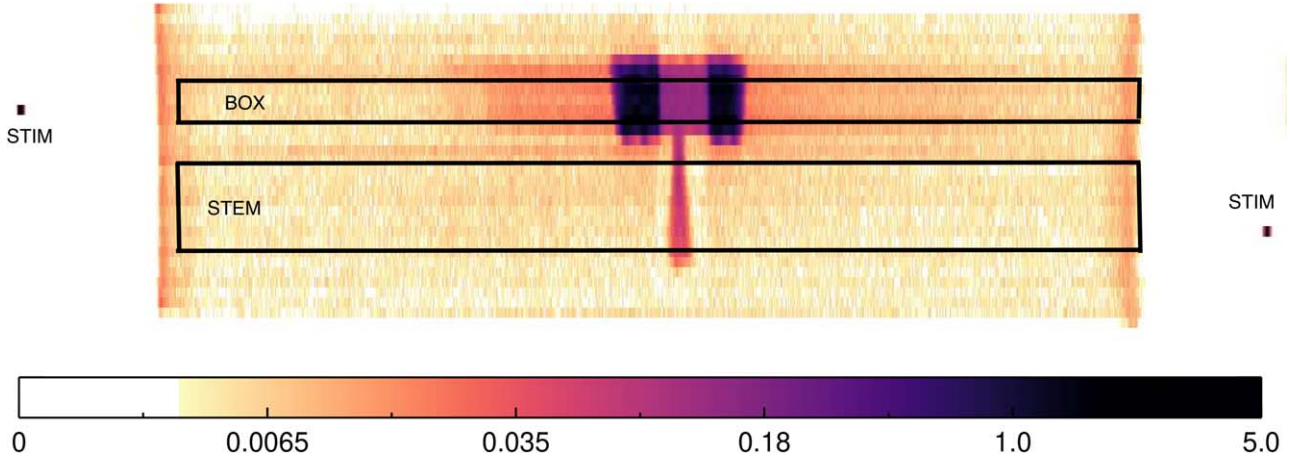

Figure 3. Detector image of one of our diffuse background observations, with the instrumental STIM pulses seen on either side of the image. The scale is in units of counts pixel^{-1} s^{-1}. Wavelength increases to the right with the illuminated region spanning the range from 520 to 1870 Å. Lyα is at the center of the image with much of the background due to instrumental scattering and dark counts. The Stem is identified in the lower part of the image, and the Box in the upper part.

3. Data Analysis

3.1. Overview

We used an identical data analysis procedure for the entire data set of CUVB observations. We began with the Alice histogram data from the KEM2 mission (S. A. Stern et al. 2025), archived at the NASA Planetary Data System (https://pds-smallbodies.astro.umd.edu/data_sb/missions/nh-kem/index.shtml). The primary contributors to the signal are instrumental dark current, largely due to fast particles from the onboard radioisotope thermoelectric generator (RTG) and internal scattering of the intense Lyα line across the detector. We describe the identification and subtraction of these two components of the overall signal in Sections 3.2 and 3.3. The calculations were done in a count space to avoid biasing by the calibration curve.

3.2. Dark Counts

As discussed above, measurements of the dark count with the aperture door closed have been taken since the beginning of observations in 2007, with a systematic effort to interleave observations of the sky with dark measurements in the astrophysical program in 2023 (Table 3). There is some variation in the dark rate as a function of observation year (Figure 4), and we have used the dark count of the appropriate year in our dark subtraction. The errors in the dark spectrum were calculated assuming photon statistics (square root of the total number of counts) and have been taken into account in the error analysis.

The shape of the dark spectrum is constant in the Stem, with no difference in the individual spectra from 2007 to 2023 (Figure 5). The Box data from early in the mission (2007) show significant Lyα contamination (Figure 6) that affects the region around 1216 Å and at longer wavelengths, perhaps due to contamination from the solar occultation channel (SOCC). The SOCC had a solar elongation angle of about 17 degrees during the dark exposures in 2007 and did not have a door that could be closed. We took care to ensure that the SOCC was pointed to a dark patch of sky in the 2023 observations and, indeed, the dark Box spectra from 2023 show no evidence of contamination at Lyα (Figure 6).

Table 3
Dark Observations with Alice

Year	NExp[a]	Exp.[b]	$D^{c}_{\rm STEM}$	$E^{d}_{\rm STEM}$	$D^{e}_{\rm BOX}$	$E^{f}_{\rm BOX}$
2007	3	10,800	0.00368	0.00018	0.00442	0.00029
2008	3	10,800	0.00365	0.00018	0.00434	0.00028
2010	3	10,720	0.00383	0.00019	0.00436	0.00028
2012	3	10,720	0.00372	0.00019	0.00417	0.00028
2014	3	10,720	0.00352	0.00018	0.00393	0.00027
2021	9	32,400	0.00395	0.00011	0.00472	0.00017
2023	192	691,200	0.00369	0.00002	0.00417	0.00003

Notes.
[a] Number of independent exposures.
[b] Cumulative exposure time in seconds.
[c] Mean dark from 912 to 1800 Å excluding Lyα in Stem (counts pixel^{-1} s^{-1}).
[d] Mean error from 912 to 1800 Å excluding Lyα in Stem (counts pixel^{-1} s^{-1}).
[e] Mean dark from 912 to 1800 Å excluding Lyα in Box (counts pixel^{-1} s^{-1}).
[f] Mean error from 912 to 1800 Å excluding Lyα in Box (counts pixel^{-1} s^{-1}).

3.3. Lyα Scattering Matrix

In most cases, the strongest source of diffuse emission in the sky is the resonant scattering of Lyα photons from the Sun by interplanetary hydrogen atoms. The Alice detector was masked around 1216 Å during the coating process to reduce the number of counts due to Lyα (S. A. Stern et al. 2008) but, despite this, internal scattering of the Lyα photons contaminates much of the spectrum. Although the Lyα scattering function was characterized during the ground calibration, it was difficult to simulate an aperture-filling diffuse field in the lab, and the data were not well fitted by the ground scattering function.

The strength of the Lyα line and, hence, the scattered light drops rapidly as a function of distance from the Sun (J. Murthy et al. 1999; G. R. Gladstone et al. 2018). Alice reobserved a long observation of the blank sky from 2007 (Table 4) to isolate the scattered Lyα in the spectrum. The strength of the Lyα line dropped by a factor of 3.5 between 2007, when the distance of NH from the Sun was about 8 au, and 2023, when the distance was about 57 au. There were six observations taken of the sky in 2007 and 10 in 2023, distributed as shown in Figure 7. There was little variation in the diffuse background in the Stem observations, but there was a 7.2 mag A3 V star (HIP 648) in some, but not all, of the Box observations. The

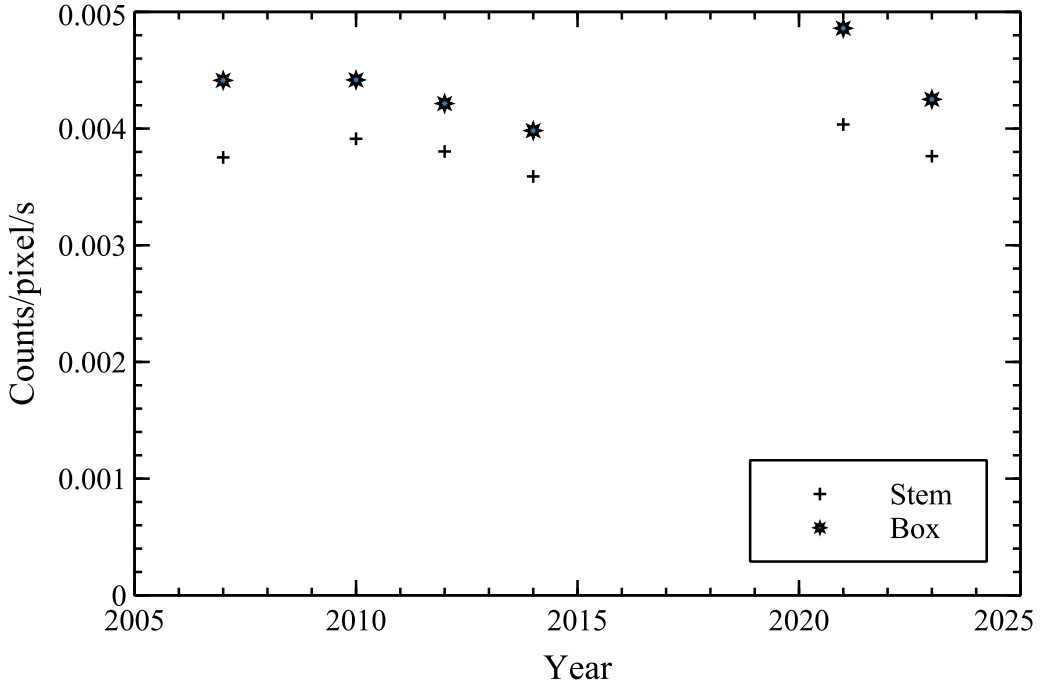

Figure 4. The average dark count rate over the Stem (+) and the Box (*) as a function of the year in which the observations were taken (Table 3). The error bars were smaller than the data points.

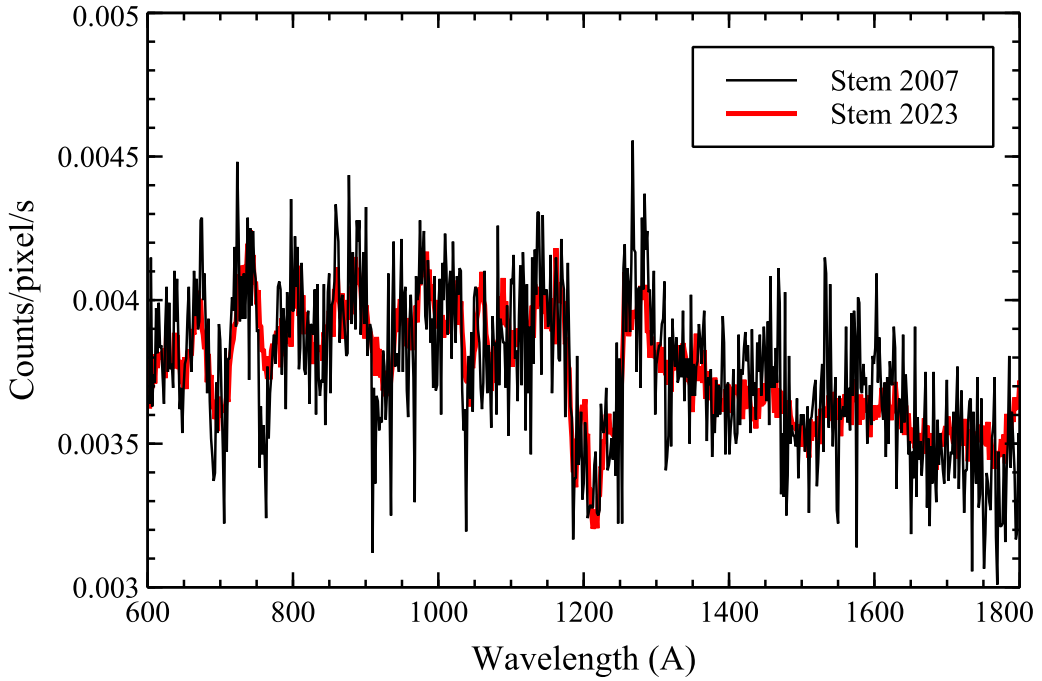

Figure 5. Spectrum of the dark counts in the Stem from 2007 (black line) and 2023 (red line). Note that there is less noise in 2023 because of the length of the dark observations (Table 3).

geometry of the observations was such that we obtained the maximum signal-to-noise when we used those observations (five observations in 2007 and seven in 2023) that included the star in deriving the Lyα scattering function for the Box.

The CUVB is the same in both sets of observations, and the scattering template is simply:

$$T = \frac{(S_{2007} - D_{2007}) - (S_{2023} - D_{2023})}{(L_{2007} - L_{2023})} \quad (2)$$

where

1. T is the Lyα scattering template (to be derived from the data).
2. S_{2007} and S_{2023} are the total signal in 2007 and 2023, respectively.
3. L_{2007} and L_{2023} are the respective counts under the Lyα line, calculated after subtraction of the dark counts.
4. D_{2007} and D_{2023} are the dark spectrum in 2007 and 2023, respectively. The dark spectrum in the Stem was the same in both the 2007 observations and the 2023 observations, and we used D_{2023} for both sets of observations.

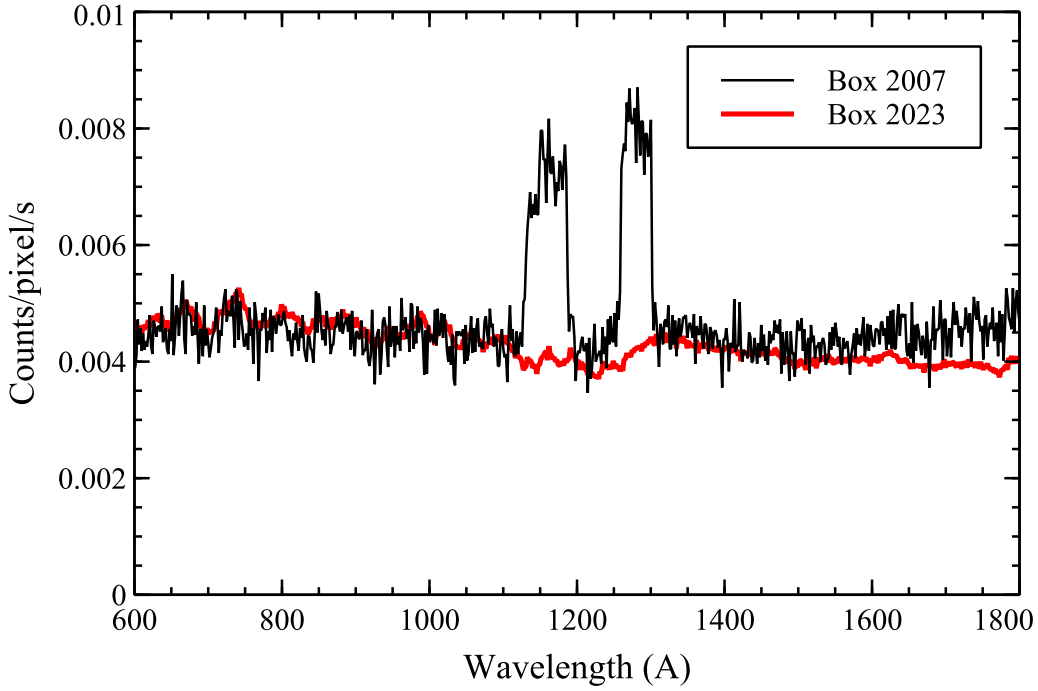

Figure 6. Spectrum of the dark counts in the Box from 2007 (black line) and 2023 (red line).

Table 4
Lyα Template

Year	l^a	b^b	N^c	Exp. Time (s)	STEM[d]	BOX[e]
2007	306.0	−36.8	6	32,400	1170	953
2023	306.0	−36.7	10	36,000	1130	879

Notes.
[a] Mean Galactic longitude of boresight.
[b] Mean Galactic latitude of boresight.
[c] Number of exposures.
[d] Mean GALEX surface brightness (photon units) in Stem aperture.
[e] Mean GALEX surface brightness (photon units) in Box aperture.

The difference between the scaled Lyα template (T) and the actual spectrum (S) is the CUVB (DGL + EBL):

$$\mathrm{CUVB} = (S - D) - L * T. \quad (3)$$

We have shown the different components of the observed spectrum in Figure 8 for the Stem and Figure 9 for the Box.

3.3.1. CUVB and Error Analysis

The CUVB (DGL + EBL) may be identified with the residual after subtracting the Lyα template and the dark count. We have plotted the CUVB for the Box (Note that the CUVB for the Box includes a small contribution from HIP 648 at the longest wavelengths) and the Stem as 1σ error bars in Figure 10 where the error bars are calculated as follows:

1. The error in the dark counts is the square root of the total number of counts in each pixel.
2. The error in each of the two observations (2007 and 2023) is the square root of the number of counts in each pixel.
3. The error in the Lyα template is the error in each of the two observations added in quadrature.
4. The final error in the CUVB is the square root of the sum of the squares of the errors in the observation, in the scaled template, and in the dark counts.

The error bars are much smaller for the Box than the Stem because the Box is much larger and is, therefore, more sensitive to diffuse radiation at the cost of spatial and spectral resolution. We have applied the same dark and template subtraction to all of our observations and will discuss the results below.

4. Results

4.1. Overview

We have calculated the CUVB in each of the Stem and Box observations separately using Equation (3). The calculations were performed in counts-space (counts s^{-1} $pixel^{-1}$) and then converted into photon units using a calibration determined through a comparison with GALEX observations (described in Section 4.2). The spectra are plotted for the Box (Figure 11), with the mean surface brightness in each band tabulated in Table 5. We have not shown the spectra from the Stem because of their poor signal-to-noise ratio. Both the Stem and the Box data are available in electronic format.

We have excluded the following observations from our analysis in the rest of this work:

1. "H2_NE" was located at a low Galactic latitude to search for molecular hydrogen fluorescence and its modeling is complex with multiple components.
2. There was a fourth-magnitude (V magnitude) B5 star near the Stem in "DCAL04."
3. There was a sixth-magnitude (V magnitude) A1 star in the Box in "NHTF01."
4. We exclude the template observation ("LYACAL").

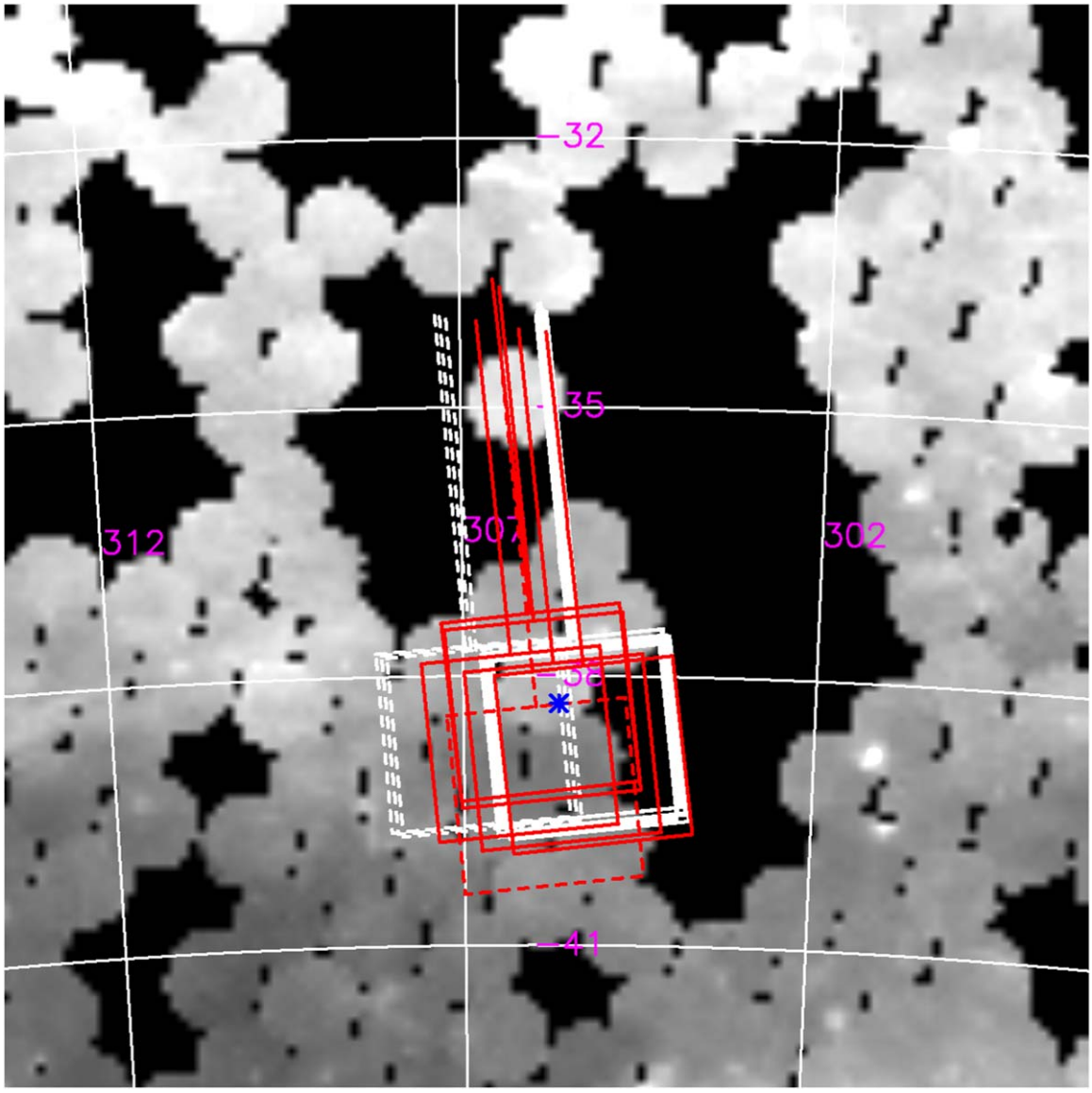

Figure 7. Diffuse FUV image from GALEX (J. Murthy 2014) in Galactic coordinates with the Alice Box and Stem observations from 2007 (red) and 2023 (white) superimposed. The dashed observations did not include the star HIP 648 (blue star) in the Box and were not used in the derivation of the Box template. Black areas show where there were no GALEX diffuse data.

4.2. Comparison with GALEX

The Alice spectrograph was calibrated on the ground with the calibration updated through stellar observations during the mission. However, it is difficult to calibrate aperture-filling diffuse sources, especially for an aperture the size of the Box, and we have used diffuse GALEX data (J. Murthy 2014) to cross-calibrate the Alice observations. We calculated the mean GALEX FUV (1536 Å) background in the Stem and the Box for each observation and compared it with the mean Alice surface brightness between 1400 and 1700 Å for each aperture. The errors in the Alice data were estimated from the mean of the errors in that range. We found an excellent correlation for both the Stem and the Box with the GALEX diffuse background values (Figure 12), but with slopes of 0.82 ± 0.14 and 0.71 ± 0.05, respectively (Table 6), reflecting both changes in the calibration over the lifetime of the mission and the difficulty in measuring the exact solid angle of the apertures. We have, therefore, rescaled the Alice spectra by these factors, assuming that a single scale factor applies over the entire Alice spectrum. There is evidence for a small offset ($\approx$23 photon units at 1σ) between GALEX and Alice, perhaps due to two-photon emission arising in the Earth's atmosphere (S. R. Kulkarni 2022).

4.3. CUVB at $\lambda < 912$ Å

Because Alice's sensitivity extends below the Lyman limit, we have used the spectral region from 600 to 800 Å to constrain the EUV radiation field, as measured from the outer solar system. The mean surface brightness over all the observations is 3.2 ± 3.0 photon units in the Box and -34.1 ± 30.6 photon units in the Stem. For radiation emerging from the field of the Alice box (4 deg^2 or 10^{-3} sr), 3.2 photon units corresponds to an EUV flux of 0.0032 photons cm^{-2} s^{-1} Å^{-1}. J. Murthy et al. (1999) also concluded that there was no emission shortward of the Lyman limit but with less certainty

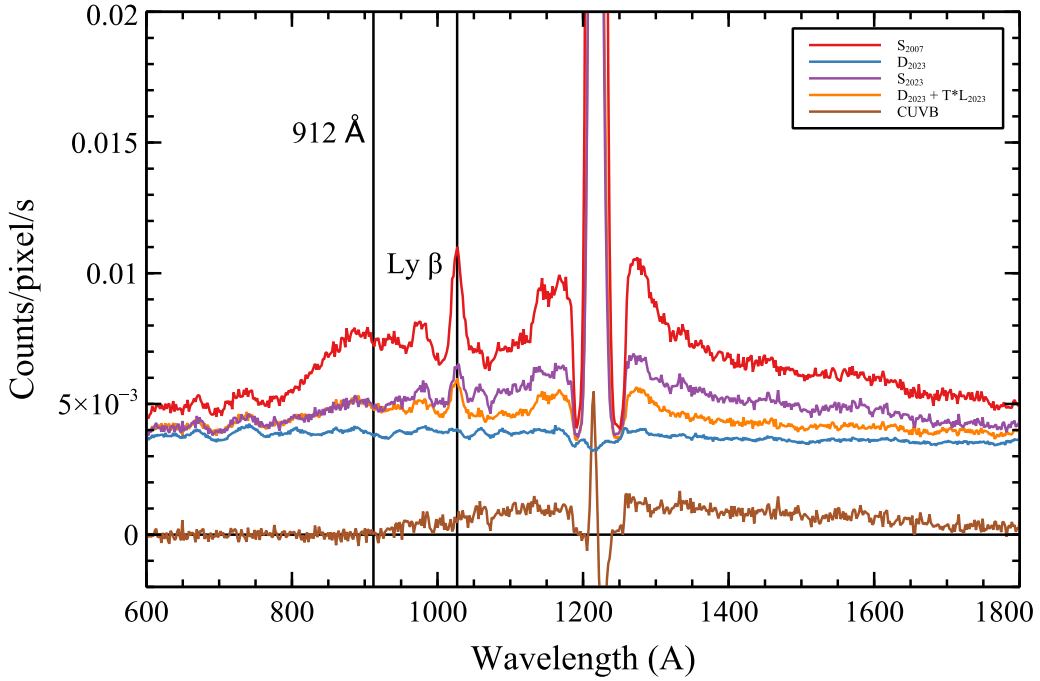

Figure 8. Different components of the template creation for the Stem. Symbols in the key are as defined in Equation (2). The Lyα scattering matrix is given by the difference between the observed spectrum in 2007 (S_{2007}) and 2023 (S_{2023}) and has to be scaled to the observed counts in the Lyα line. The CUVB is the resultant after subtraction of the scaled scattering matrix and the dark current ($D_{2023} + T \times L_{2007}$)

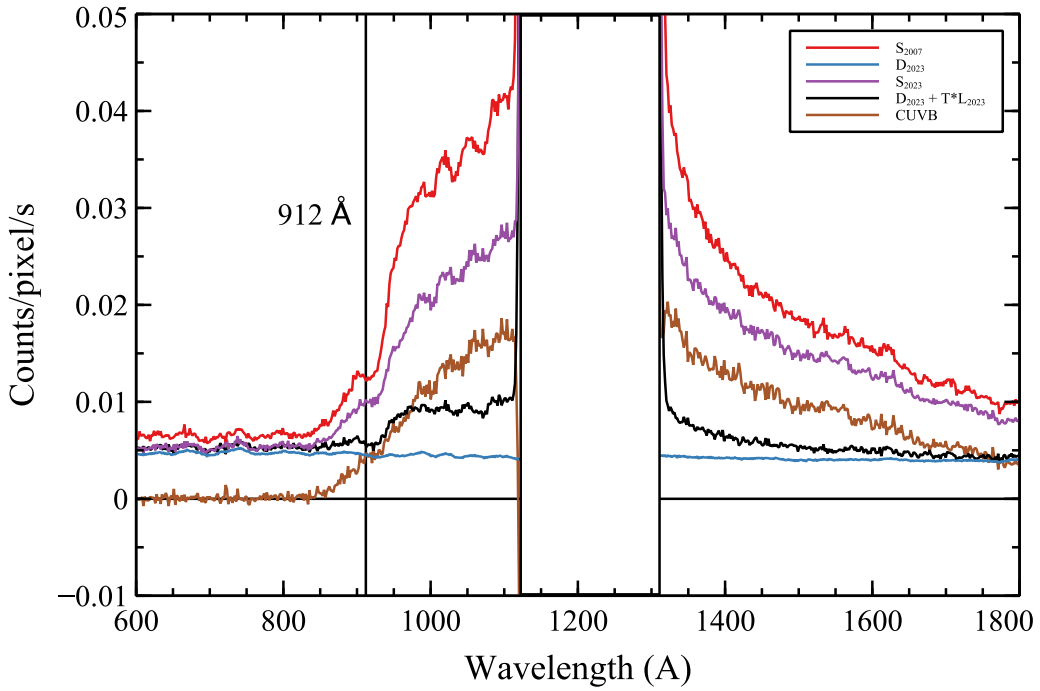

Figure 9. Different components of the template creation for the Box. Symbols in the key are as defined in Equation (2). See the caption for Figure 8.

given the relatively poor sensitivity of the Voyager ultraviolet spectrometer (UVS).

Currently, the best EUV flux limits come from studies by the Extreme Ultraviolet Explorer (EUVE) mission, which observed 54 local stars within 150 pc, mostly white dwarfs (J. Dupuis et al. 1995; J. V. Vallerga 1998). The EUVE fluxes as seen from Earth are dominated by radiation from five stars: ϵ CMa ($d = 124$ pc), β CMa (151 pc), G191-B2B (52.5 pc), HZ43A (60.3 pc), and Feige 24 (77.7 pc). The NH-Alice limit (0.0032 photons cm^{-2} s^{-1} Å^{-1}) is well below the fluxes from these stars. However, the local EUV radiation field is likely to be quite anisotropic, and the stellar EUV fluxes have been attenuated by variable absorption from the Local Interstellar Clouds. In the wavelength range observed by EUVE, the brightest WD fluxes peak at 250 Å (owing to H I and He I absorption) at 0.15–0.60 photons cm^{-2} s^{-1} Å^{-1}, dropping to 0.01–0.04 photons cm^{-2} s^{-1} Å^{-1} at 450–600 Å. By comparison, ϵ CMa has photon flux at 600–900 Å ranging from 0.6 to

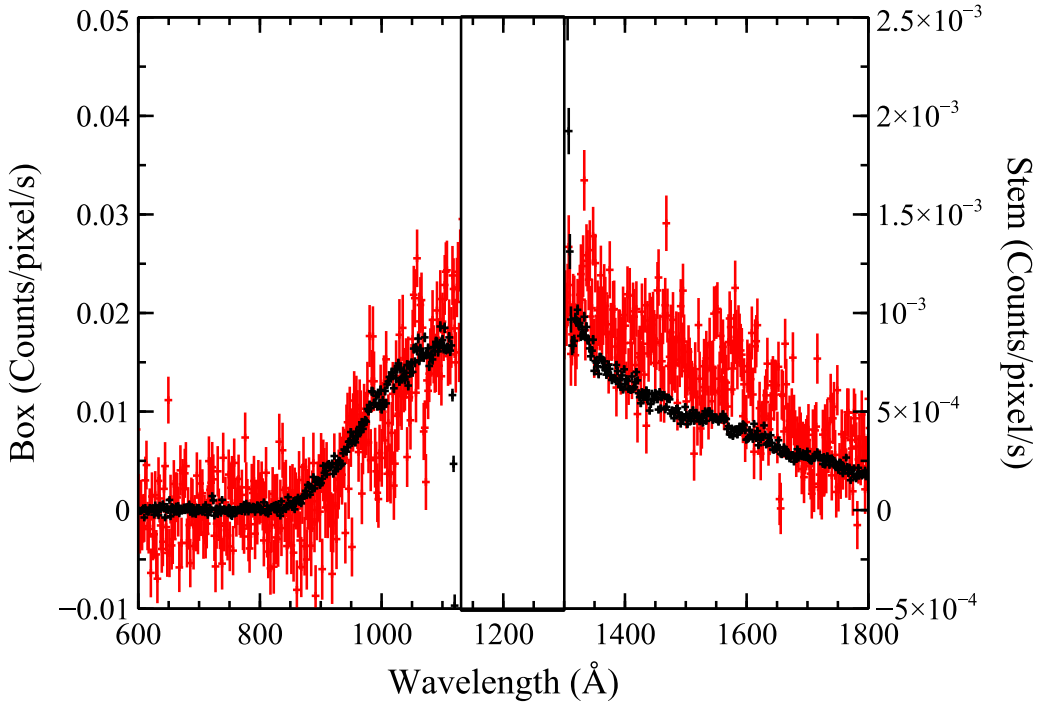

Figure 10. Derived CUVB in the Stem (red) and Box (black), plotted as 1σ error bars, where the derivation of the errors is discussed in Section 3.3.1. The solid angle subtended by the Stem is $\frac{1}{20}$ that of the Box, and this is reflected in the observed count rate. We have not shown the region immediately around the Lyα line where the subtraction of the intense Lyα line is uncertain.

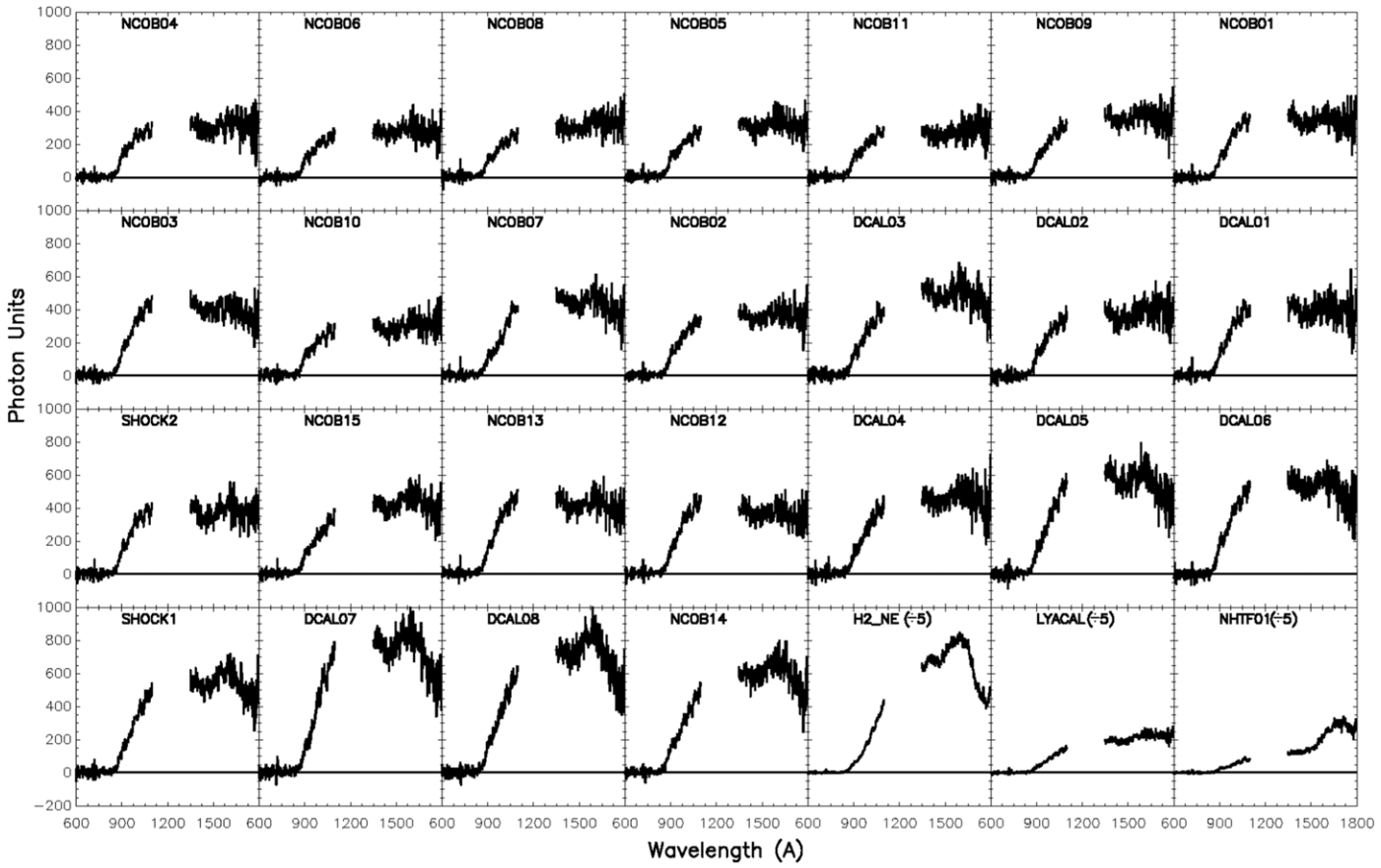

Figure 11. Box spectrum for each of the fields plotted as a function of wavelength (600–1800 Å). The spectra are ordered by the mean Planck $E(B-V)$ in the Box, except for the last three spectra, and are labeled as per Table 2. The surface brightness in the last three spectra has been divided by 5 for plotting purposes and is not used in the analysis (see text). The data are available in electronic format.

(The data used to create this figure are available in the online article.)

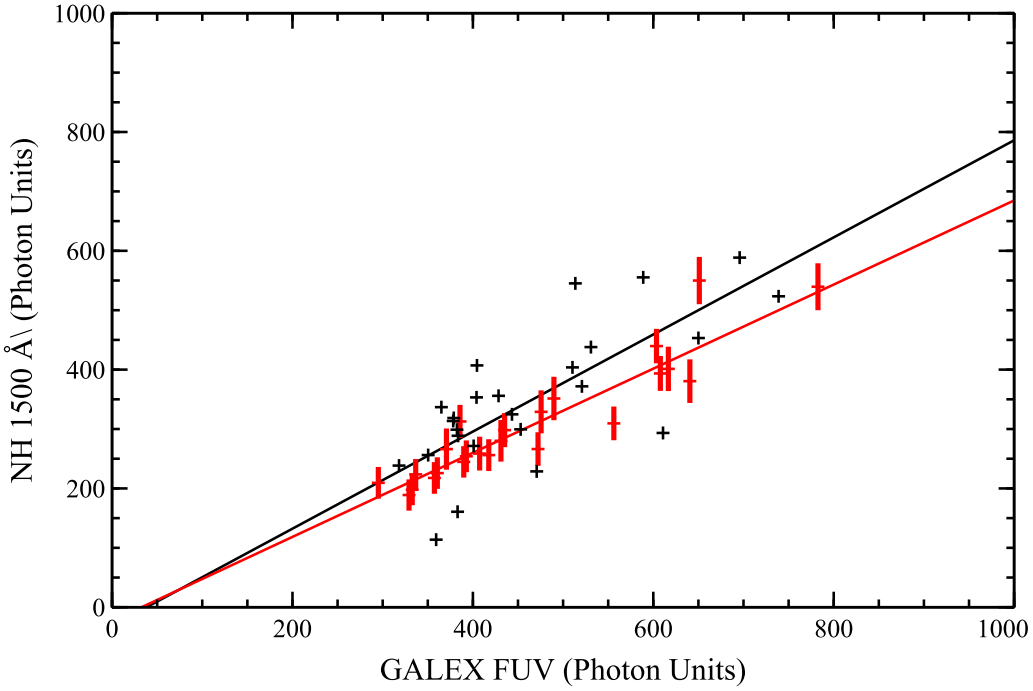

Figure 12. Stem (black) and Box (red) Alice surface brightness between 1350 Å and 1800 Å compared to the mean GALEX surface brightness in the FUV band. The best-fit lines are NH = $0.82G - 31.2$ for the Stem (black line) and NH = $0.71G - 23.2$ for the Box (red line), where NH is the observed Alice surface brightness and G is the GALEX surface brightness (Table 6). We have shown 1σ error bars for the Box but not for the Stem to avoid clutter in the plot.

Table 5
Observed Surface Brightness in Box

Target	$E(B-V)$[a]	S^{b}_{1000}	S^{c}_{1500}
NCOB04	0.011	245 ± 15	307 ± 37
NCOB06	0.011	204 ± 15	279 ± 36
NCOB08	0.011	204 ± 14	315 ± 36
NCOB05	0.013	222 ± 15	318 ± 37
NCOB11	0.013	221 ± 15	266 ± 37
NCOB09	0.013	241 ± 15	361 ± 37
NCOB01	0.013	268 ± 15	345 ± 37
NCOB03	0.014	335 ± 16	398 ± 38
NCOB10	0.014	224 ± 15	295 ± 37
NCOB07	0.015	270 ± 15	441 ± 39
NCOB02	0.016	263 ± 15	358 ± 37
DCAL03	0.017	287 ± 20	496 ± 51
DCAL02	0.017	272 ± 20	376 ± 48
NHTF01	0.018	276 ± 16	993 ± 47
DCAL01	0.018	311 ± 20	395 ± 49
SHOCK2	0.020	314 ± 16	376 ± 39
NCOB15	0.021	252 ± 16	437 ± 40
NCOB13	0.024	357 ± 16	421 ± 40
NCOB12	0.025	337 ± 17	365 ± 40
DCAL04	0.026	291 ± 20	464 ± 51
DCAL05	0.027	373 ± 21	566 ± 52
DCAL06	0.039	387 ± 21	537 ± 51
SHOCK1	0.042	342 ± 16	555 ± 41
DCAL07	0.053	465 ± 22	776 ± 56
DCAL08	0.055	408 ± 21	762 ± 55
NCOB14	0.058	344 ± 16	620 ± 40
LYACAL	0.078	486 ± 38	1055 ± 100
H2_NE	0.594	1084 ± 20	3642 ± 65

Notes.
[a] Mean Planck $E(B-V)$ in Box (mag).
[b] Surface brightness (912–1150 Å) in photon units (ph cm^{-2} s^{-1} sr^{-1} Å^{-1}).
[c] Surface brightness (1400–1800 Å) in photon units (ph cm^{-2} s^{-1} sr^{-1} Å^{-1}).

Table 6
Galex/Alice Scale Factor

	r[a]	Slope	Offset[b]
Stem	0.742	0.82 ± 0.14	−31.2 ± 66.4
Box	0.932	0.71 ± 0.05	−23.2 ± 24.1

Notes.
[a] Correlation coefficient.
[b] photon units

1.1 photons cm^{-2} s^{-1} Å^{-1}. This is consistent with a local EUV radiation field that is highly directional and dominated by just a few stars, as noted by J. Murthy & D. J. Sahnow (2004) using observations at 1000–1200 Å from the FUSE spacecraft.

We can also compare the 3.2 photon units limit to the low-redshift metagalactic ionizing background flux, which has been estimated to be $J_0 = 1.3^{+0.8}_{-0.5} \times 10^{-23}$ erg cm^{-2} s^{-1} Hz^{-1} sr^{-1} (J. M. Shull et al. 1999), which translates to 2.15 photon units in wavelength distribution units. The ionizing fluxes decline at shorter wavelengths and will be somewhat lower at 600 Å. The metagalactic LyC photons are unlikely to propagate to the Galactic disk plane owing to strong H I absorption.

4.4. Offsets at Zero Reddening

M. S. Akshaya et al. (2019) found that GALEX FUV observations were tightly correlated with the Planck $E(B-V)$ (Planck Collaboration et al. 2014) and with the 100 μm emission from D. J. Schlegel et al. (1998), with zero-offsets of 230–290 photon units at both poles. They noted that these offsets were much greater than the 73 ± 16 photon units attributed to the integrated light of galaxies in the FUV (S. P. Driver et al. 2016), in agreement with earlier observations of the CUVB at the Galactic poles (Table 1).

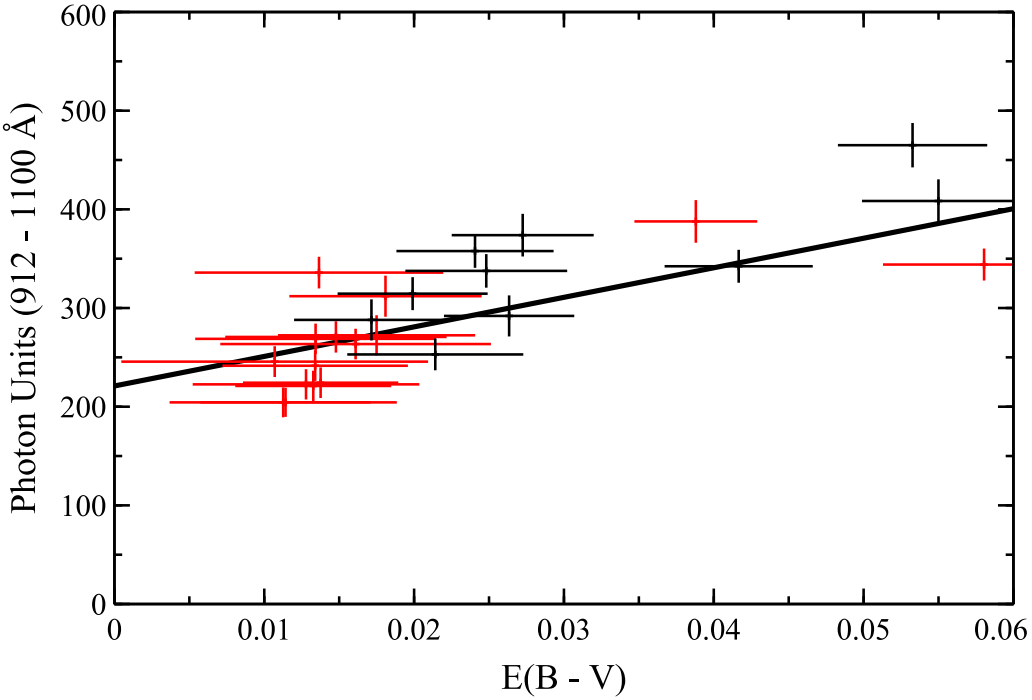

Figure 13. Mean surface brightness in the Box from 912 to 1100 Å as a function of the $E(B-V)$ with 1σ errors. Red points are near the south Galactic pole, and black points are near the north Galactic pole. The line represents the best fit to the data with SB = $2994E(B-V)+221$ photon units (Table 5), where SB is the observed surface brightness.

They attributed the excess emission to a new component of the diffuse background, but one not associated with interstellar dust (R. C. Henry et al. 2015). Similar conclusions were drawn by E. T. Hamden et al. (2013), who presented an all-sky GALEX map with a nonscattered isotropic component of diffuse FUV emission at a level of 300 photon units.

The Alice spectra offer an opportunity to test this correlation from a location near the edge of the solar system, where we will only see emission from Galactic and extragalactic sources. We first divided the Alice spectra into two bands (912–1100 Å and 1400–1700 Å) and found the mean surface brightness in each band for the Stem and the Box, with the error assumed to be the mean error over the bandpass. Note that the line width of the Box (FWHM 172 Å) meant that we had to integrate to 850 Å to include all the signal from the short-wavelength band. The bandpass-averaged surface brightness is well correlated with the reddening in each aperture (Figures 13 and 14), where the reddening was obtained from the mean of the Planck $E(B-V)$ over each aperture. The uncertainty in the $E(B-V)$ was also taken from the Planck data and was approximately 0.005 mag in these fields.

We performed a least-squares fit between the UV surface brightening and the reddening, taking into account the uncertainties in both the Alice values and the $E(B-V)$, and the resultant slopes and offsets are tabulated in Table 7. As expected, we find similar values from both the Stem and the Box but will focus on the Box results because of their much higher signal-to-noise ratio. The Box spectra are of sufficiently high quality that we can fit the offset, again using a least-squares fit, at each wavelength (Figure 15). This is the first measurement of the zero-offset in the wavelength region between 912 and 1100 Å and is consistent with the <200 photon units found through Voyager observations of the north Galactic pole from 912 to 1100 Å (J. B. Holberg 1986), considering the relatively poor sensitivity of the Voyager UVS. The offsets are close to flat between 1400 and 1800 Å at a level of about 290 photon units, confirming previous observations made from Earth orbit (Table 1). Although it appears that the offsets decrease almost linearly from 1100 to 912 Å, we caution that this may be an artifact of the Box line width of 172 Å. There is no significant difference between the offsets determined from observations in the southern hemisphere to those from the northern hemisphere (Figure 16). We will discuss the likely contributors below, but note that known sources amount to less than half of the total observed offset.

The EBL in the UV is generally thought to be composed primarily of the integrated light of galaxies (S. P. Driver et al. 2016; K. Mattila & P. Väisänen 2019). This has been estimated by several previous surveys, with values ranging from 73 to 195 photon units in the GALEX FUV band. J. P. Gardner et al. (2000) used Space Telescope Imaging Spectrograph (STIS) observations of portions of the North and South Hubble Deep Fields and a parallel field near the North Deep Field down to AB magnitude 29–30 to find a range from 144 to 195 photon units for the EBL, specifically quoting both lower limits $\Phi_\lambda \geqslant 144^{+28}_{-19}$ photon units and upper limits $\Phi_\lambda \leqslant 195^{+59}_{-39}$ photon units. A subsequent analysis of the Hubble Ultraviolet Ultra-Deep Field (S. P. Driver et al. 2016) in the FUV (1530 Å band) quoted a value of 1.45 ± 0.27 nW m^{-2} sr^{-1}, corresponding to 73 ± 14 photon units. Their analysis included number counts of galaxies from GALEX extending to AB magnitude 23.8, yielding 34 ± 5 photon units (C. K. Xu et al. 2005); their survey extended 5 mag deeper, to AB = 29–30, using the solar-blind channel of the HST Advanced Camera for Surveys. Both HST surveys showed that galaxy counts increase at AB > 23 mag, flattening from AB = 26 to 30. We have adopted the value of 73 ± 14 photon units from S. P. Driver et al. (2016) for the contribution to the FUV background from

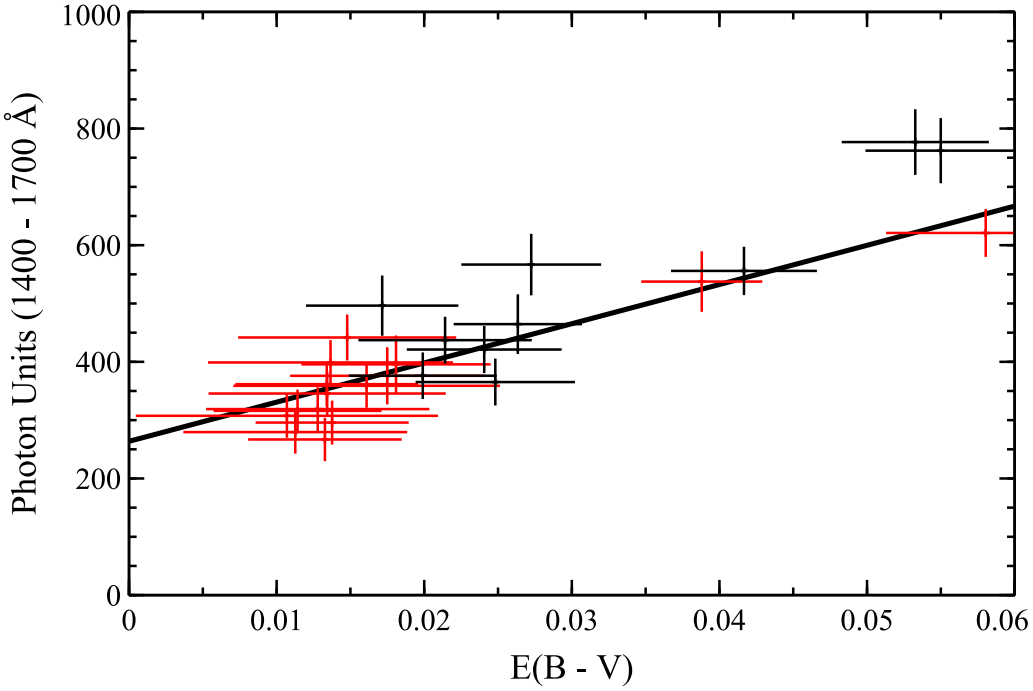

Figure 14. Mean surface brightness in the Box from 1400 to 1700 Å as a function of the $E(B-V)$ with 1σ errors. Red points are near the south Galactic pole, and black points are near the north Galactic pole. The line represents the best fit to the data with SB = $6723E(B-V)+264$ photon units (Table 5), where SB is the observed surface brightness.

Table 7
Correlation with $E(B-V)$

Quantity	r[a]	Slope[b]	Offset[c]	χ^2
		912–1100 Å		
STEM EBV	0.596	2213.8 ± 1693.7	172.3 ± 47.6	0.15
BOX EBV	0.807	2994.4 ± 446.1	221.0 ± 11.2	2.92
		1400–1700 Å		
STEM EBV	0.702	6554.3 ± 4612.4	257.4 ± 129.8	0.08
BOX EBV	0.909	6722.5 ± 909.0	263.7 ± 24.1	1.17

Notes.
[a] Correlation coefficient.
[b] photon units mag^{-1}.
[c] photon units.

galaxy counts at high Galactic latitudes and used the spectrum from S. Koushan et al. (2021).

Only hot (O and B) stars can contribute significantly in the Alice spectral range, particularly in the 900–1100 Å band. We checked each field using Astroquery (A. Ginsburg et al. 2019) for the presence of any O, B, or A stars near the Box in the Simbad database (M. Wenger et al. 2000). Only four fields included A stars, with no O or B stars, with an effective contribution of about 30 photon units at 1500 Å and nothing at 1000 Å. These stars will be included in the GALEX point source catalog (L. Bianchi et al. 2018), which is complete to an AB magnitude of 19.9 in the FUV. Stars in the catalog contribute a mean of 26.7 ± 10.5 photon units in the GALEX FUV band (1350–1800 Å). We estimated the contribution of fainter stars to 30th magnitude using TRILEGAL (L. Girardi et al. 2005) and found that the expected contribution was equivalent to one B1 star per square degree with an AB magnitude of 17.7, equivalent to a diffuse signal of 19.1 ± 2 photon units and 13.6 ± 2 photon units at 1000 Å and 1500 Å, respectively. We assumed that the stars from the L. Bianchi et al. (2018) catalog have a similar spectrum and found a total contribution of 56.2 ± 11 photon units at 1000 Å and 40.3 ± 11 photon units at 1500 Å from resolved and unresolved stars.

O VI (1032/1038 Å) emission from the Galactic halo will contribute 4450 ± 950 ph cm^{-2} s^{-2} sr^{-1} (W. V. D. Dixon et al. 2001; R. L. Shelton et al. 2001; Y.-S. Jo et al. 2019) and C IV (1548/1550 Å) will contribute approximately 5000 ± 800 ph cm^{-2} s^{-2} sr^{-1} (C. Martin et al. 1990; Y.-S. Jo et al. 2019). Because of the 172 Å FWHM of the Box, these lines are spread over the entire spectral range and correspond to a contribution of about 20 photon units in each band. Finally, two-photon emission from the warm ISM will contribute an additional 20 photon units (S. R. Kulkarni 2022). There may also be small contributions from H_2 fluorescence in the Lyman bands between 1330 and 1620 Å if some fields contain trace amounts of H_2 in the cirrus clouds (K. Gillmon & J. M. Shull 2006; Y.-S. Jo et al. 2017).

We have plotted the different components discussed above in Figure 15, finding that the observed radiation is at least double the sum of all the contributors over the entire spectral range. We have, as yet, no explanation for the excess radiation. Based on spatial cross-correlation with redshift surveys of extragalactic objects, Y.-K. Chiang et al. (2019) identified a monopole contribution of 90 $(+28, -16)$ Jy sr^{-1} (approximately 91 photon units) of FUV background associated with extragalactic objects. They argue that an extragalactic origin to the unaccounted foreground can be ruled out by their clustering analysis.

5. Implications for Future Missions

Future experiments relevant to the FUV background include NASA's recently selected mission UVEX (UltraViolet

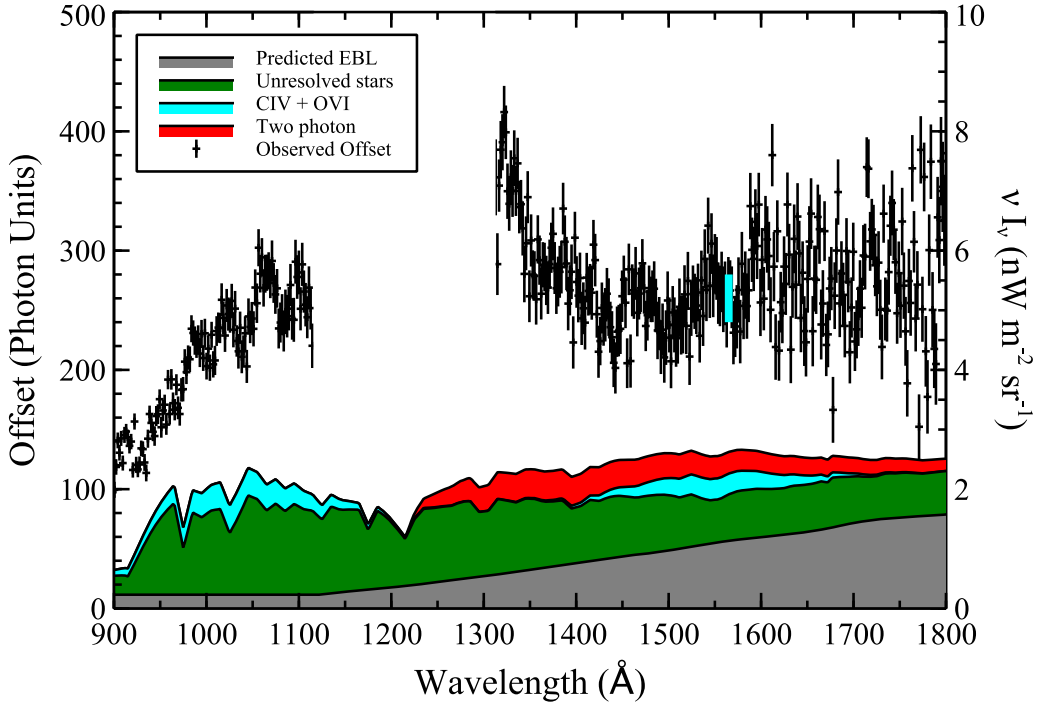

Figure 15. Offsets at zero reddening plotted as 1σ error bars for the Box. The discontinuity from 1100 to 1350 Å is because we have blanked out the section where uncertainties in the subtraction of the Lyα template dominate the errors. Components of the diffuse radiation field are plotted in order from the bottom: EBL (filled gray) from S. Koushan et al. (2021), unresolved stars (filled green), O VI and C IV line emission (cyan), and two-photon emission (red). The cyan bar represents the GALEX offset found by M. S. Akshaya et al. (2018). See text for discussion.

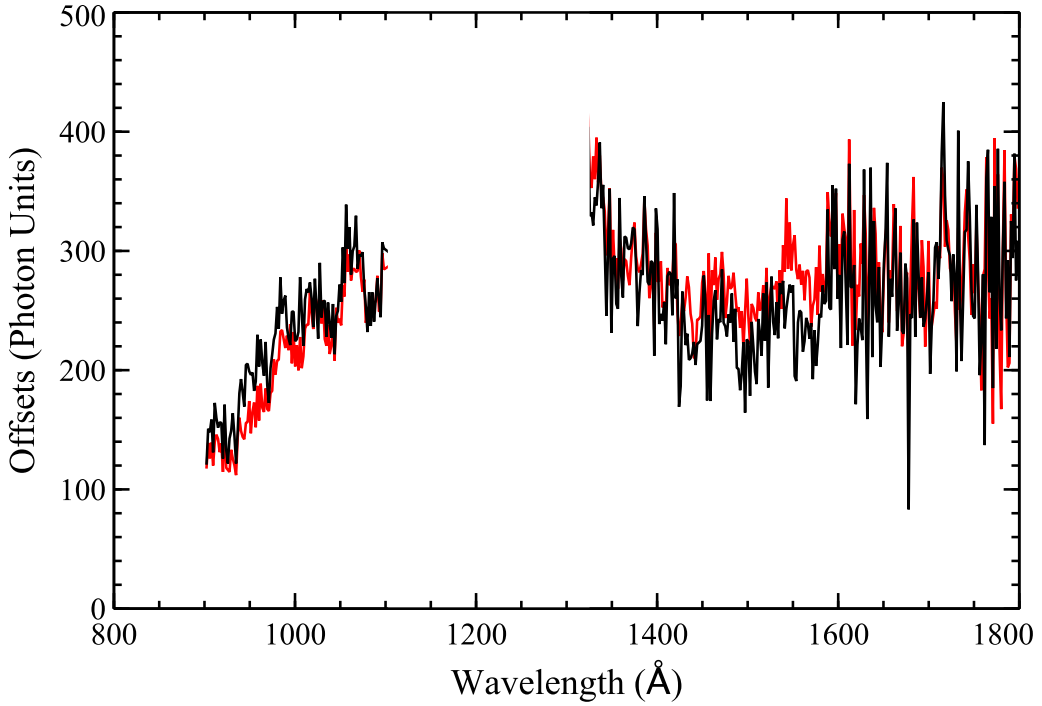

Figure 16. Offsets for the northern observations (black) and the southern observations (red).

EXplorer) to survey ultraviolet light across the entire sky, providing insight into how galaxies and stars evolve. UVEX is targeted to launch in 2030 as NASA's next Astrophysics Medium-Class Explorer mission (https://www.uvex.caltech.edu). In addition to its capability to quickly point toward sources of ultraviolet light in the Universe, UVEX will conduct a highly sensitive all-sky survey at both FUV and NUV wavelengths, with a sensitivity 50 times better than GALEX. UVEX will have a wide-field ($3.^{\circ}5 \times 3.^{\circ}5$) two-band ultraviolet imager covering the FUV (1390–1900 Å) and NUV (2030–2700 Å) with $2''$ point-spread function. Ultraviolet spectroscopy will be obtained with a two-degree long

Table 8
Components of Offsets

Source	Offset[a]	References
	912–1100 Å	
Observed	221 ± 11	This work
EBL	<10	S. Koushan et al. (2021)
Stars	56 ± 11	L. Girardi et al. (2005)
		L. Bianchi et al. (2018)
O VI	22 ± 5	R. L. Shelton et al. (2001)
Excess	133 ± 17	
	1400–1700 Å	
Observed	264 ± 24	This work
EBL	73 ± 16	S. P. Driver et al. (2016)
Stars	40 ± 11	L. Girardi et al. (2005)
		L. Bianchi et al. (2018)
C IV	25 ± 4	C. Martin & S. Bowyer (1990)
Two-photon	23 ± 3	S. R. Kulkarni (2022)
Excess	103 ± 31	

Note.
[a] Photon units.

multiwidth slit spectrometer covering wavelengths from 1150 Å to 2650 Å. In its wide elliptical orbit around the Earth (17–59R_E) and synoptic observations, UVEX should be above the Earth's exospheric contributions (Kulkarni 2022) and able to monitor (and subtract out) most of the solar contributions to the FUV background. As with the cosmic X-ray background, it is likely that UVEX will uncover a more complex picture of the spatial and spectral signatures of the CUVB.

6. Summary

We have observed 25 targets near the Galactic poles with the Alice spectrograph on the New Horizons spacecraft. These target fields were complementary to LORRI observations of the COB (M. Postman et al. 2024). The CUVB is linearly correlated with the interstellar reddening with offsets of 221 ± 11 photon units at 1000 Å and 264 ± 24 at 1500 Å, consistent with earlier observations of the offsets at the Galactic Poles and significantly greater than the sum of the known sources (Table 8). The excess surface brightness over all the identified sources is 133 ± 17 photon units at 1000 Å and 103 ± 31 photon units at 1500 Å.

There is no background radiation detected shortward of the H I Lyman limit in any of the high-latitude fields, at a level of 3.2 ± 3.0 photon units between 600 and 800 Å. This corresponds to an EUV flux of 0.003 photons cm^{-2} s^{-1} $Å^{-1}$, suggesting that the EUV emission from the bright stellar sources seen by EUVE (J. Dupuis et al. 1995; J. V. Vallerga 1998) is highly localized.

Importantly, we have found that there is, at most, an offset of −23 ± 24 photon units between the Alice observations and GALEX data at 1500 Å; that is, the contributions to the diffuse background are close to zero from the Earth's atmosphere. Hence, observations of the FUV (1300–1800 Å) may very well be made from spacecraft in low Earth orbit, such as GALEX or the future UVEX mission (see below). This is not true for observations shortward of 1200 Å, where scattering from the intense Lyα line will dominate the signal unless we observe from the outer solar system.

Acknowledgments

We thank NASA for funding and continued support of the New Horizons mission, which were required to obtain the present observations. No New Horizons NASA funds were used for the analysis and writing of this paper. The data presented were obtained during the second Kuiper Extended Mission of New Horizons. We thank Kwang-Il Seon, Jonathan Gardner, Harry Teplitz, and Shri Kulkarni for useful discussions. Some of the data presented in this paper were obtained from the Mikulski Archive for Space Telescopes (MAST). STScI is operated by the Association of Universities for Research in Astronomy, Inc., under NASA contract NAS5-26555. Support for MAST for non-HST data is provided by the NASA Office of Space Science via grant NNX13AC07G and by other grants and contracts. This research has made use of the SIMBAD database, CDS, Strasbourg Astronomical Observatory, France. All costs associated with the publication of this paper were borne by NASA's Maryland Space Grant Consortium.

Software: GnuDataLanguage (A. Coulais et al. 2010; A. Coulais et al. 2011; J. Park et al. 2022), Fawlty Language http://www.flxpert.hu/fl/, TRILEGAL (L. Girardi et al. 2005).

ORCID iDs

Jayant Murthy https://orcid.org/0000-0003-4034-5137
Marc Postman https://orcid.org/0000-0002-9365-7989
Joel Wm. Parker https://orcid.org/0000-0002-3672-0603
Seth Redfield https://orcid.org/0000-0003-3786-3486
G. Randall Gladstone https://orcid.org/0000-0003-0060-072X
Pontus Brandt https://orcid.org/0000-0002-4644-0306
Kelsi N. Singer https://orcid.org/0000-0003-3045-8445
S. Alan Stern https://orcid.org/0000-0001-5018-7537

References

Akshaya, M. S., Murthy, J., Ravichandran, S., Henry, R. C., & Overduin, J. 2018, ApJ, 858, 101
Akshaya, M. S., Murthy, J., Ravichandran, S., Henry, R. C., & Overduin, J. 2019, MNRAS, 489, 1120
Anderson, R. C., Henry, R. C., Brune, W. H., Feldman, P. D., & Fastie, W. G. 1979, ApJ, 234, 415
Barcons, X., & Fabian, A. C. 1992, The X-Ray Background (Cambridge: Cambridge Univ. Press)
Bennett, C. L., Halpern, M., Hinshaw, G., et al. 2003, ApJS, 148, 1
Bianchi, L., de la Vega, A., Shiao, B., & Bohlin, R. 2018, Ap&SS, 363, 56
Bowyer, S. 1991, ARA&A, 29, 59
Carleton, T., Windhorst, R. A., OBrien, R., et al. 2022, AJ, 164, 170
Cheng, A. F., Weaver, H. A., Conard, S. J., et al. 2008, SSRv, 140, 189
Chiang, Y.-K., Ménard, B., & Schiminovich, D. 2019, ApJ, 877, 150
Coulais, A., Schellens, M., Gales, J., et al. 2010, in ASP Conf. Ser. 434, Astronomical Data Analysis Software and Systems XIX, ed. Y. Mizumoto, K.-I. Morita, & M. Ohishi (San Francisco, CA: ASP), 187
Coulais, A., Schellens, M., Gales, J., et al. 2011, arXiv:1101.0679
Cravens, T. E. 2000, ApJL, 532, L153
Dicke, R. H., Peebles, P. J. E., Roll, P. J., & Wilkinson, D. T. 1965, ApJ, 142, 414
Dixon, W. V. D., Sallmen, S., Hurwitz, M., & Lieu, R. 2001, ApJL, 552, L69
Driver, S. P., Andrews, S. K., Davies, L. J., et al. 2016, ApJ, 827, 108
Dupuis, J., Vennes, S., Bowyer, S., Pradhan, A. K., & Thejll, P. 1995, ApJ, 455, 574
Feldman, P. D., Brune, W. H., & Henry, R. C. 1981, ApJL, 249, L51
Frisch, P. C., Redfield, S., & Slavin, J. D. 2011, ARA&A, 49, 237
Galeazzi, M., Chiao, M., Collier, M. R., et al. 2014, Natur, 512, 171
Gardner, J. P., Brown, T. M., & Ferguson, H. C. 2000, ApJL, 542, L79
Giacconi, R., Gursky, H., Paolini, F. R., & Rossi, B. B. 1962, PhRvL, 9, 439

Gillmon, K., & Shull, J. M. 2006, ApJ, 636, 908
Ginsburg, A., Sipőcz, B. M., Brasseur, C. E., et al. 2019, AJ, 157, 98
Girardi, L., Groenewegen, M. A. T., Hatziminaoglou, E., & da Costa, L. 2005, A&A, 436, 895
Gladstone, G. R., Pryor, W. R., Stern, S. A., et al. 2018, GeoRL, 45, 8022
Hamden, E. T., Schiminovich, D., & Seibert, M. 2013, ApJ, 779, 180
Hayakawa, S., Yamashita, K., & Yoshioka, S. 1969, Ap&SS, 5, 493
Henry, R. C. 1991, ARA&A, 29, 89
Henry, R. C., Feldman, P. D., Fastie, W. G., & Weinstein, A. 1978, ApJ, 223, 437
Henry, R. C., & Murthy, J. 1993, ApJL, 418, L17
Henry, R. C., Murthy, J., Overduin, J., & Tyler, J. 2015, ApJ, 798, 14
Henry, R. C., Swandic, J. R., Shulman, S. D., & Fritz, G. 1977, ApJ, 212, 707
Holberg, J. B. 1986, ApJ, 311, 969
Jakobsen, P., Bowyer, S., Kimble, R., et al. 1984, A&A, 139, 481
Jo, Y.-S., Seon, K.-I., Min, K.-W., Edelstein, J., & Han, W. 2017, ApJS, 231, 21
Jo, Y.-S., Seon, K.-i., Min, K.-W., et al. 2019, ApJS, 243, 9
Joubert, M., Deharveng, J. M., Cruvellier, P., Masnou, J. L., & Lequeux, J. 1983, A&A, 128, 114
Jura, M. 1979, ApJ, 227, 798
Kollmeier, J. A., Weinberg, D. H., Oppenheimer, B. D., et al. 2014, ApJ, 789, L32
Korngut, P. M., Kim, M. G., Arai, T., et al. 2022, ApJ, 926, 133
Koushan, S., Driver, S. P., Bellstedt, S., et al. 2021, MNRAS, 503, 2033
Kulkarni, S. R., & Shull, J. M. 2023, PASP, 135, 124301
Kulkarni, S. R. 2022, PASP, 134, 084302
Lallement, R. 2004, A&A, 422, 391
Lallement, R., Welsh, B., Vergely, J. L., Crifo, F., & Sfeir, D. 2003, A&A, 411, 447
Lauer, T. R., Postman, M., Weaver, H. A., et al. 2021, ApJ, 906, 77
Lauer, T. R., Postman, M., Spencer, J. R., et al. 2022, ApJL, 927, L8
Lillie, C. F., & Witt, A. N. 1976, ApJ, 208, 64
Martin, C., & Bowyer, S. 1990, ApJ, 350, 242
Martin, C., Hurwitz, M., & Bowyer, S. 1990, ApJ, 354, 220
Matsuura, S., Shirahata, M., Kawada, M., et al. 2011, ApJ, 737, 2
Mattila, K., & Väisänen, P. 2019, ConPh, 60, 23
Mattila, K., Väisänen, P., Lehtinen, K., von Appen-Schnur, G., & Leinert, C. 2017, MNRAS, 470, 2152
Miville-Deschênes, M. A., & Lagache, G. 2005, ApJS, 157, 302
Murthy, J. 2009, Ap&SS, 320, 21
Murthy, J. 2014, ApJS, 213, 32
Murthy, J. 2016, MNRAS, 459, 1710
Murthy, J., Conn Henry, R., & Holberg, J. B. 2012, ApJS, 199, 11
Murthy, J., Hall, D., Earl, M., Henry, R. C., & Holberg, J. B. 1999, ApJ, 522, 904
Murthy, J., Henry, R. C., & Sujatha, N. V. 2010, ApJ, 724, 1389
Murthy, J., & Sahnow, D. J. 2004, ApJ, 615, 315
Onaka, T., & Kodaira, K. 1991, ApJ, 379, 532
Paresce, F., McKee, C. F., & Bowyer, S. 1980, ApJ, 240, 387
Park, J., Duvert, G., Coulais, A., et al. 2022, JOSS, 7, 4633
Peebles, P. J. E. 2020, Principles of Physical Cosmology (Princeton, NJ: Princeton Univ. Press)
Pence, W. D., Chiappetti, L., Page, C. G., Shaw, R. A., & Stobie, E. 2010, A&A, 524, A42
Penzias, A. A., & Wilson, R. W. 1965, ApJ, 142, 419
Planck Collaboration, Abergel, A., Ade, P. A. R., et al. 2014, A&A, 571, A11
Planck Collaboration, Ade, P. A. R., Aghanim, N., et al. 2016, A&A, 586, A132
Planck Collaboration VI 2020, A&A, 641, A6
Postman, M., Lauer, T. R., Parker, J. W., et al. 2024, ApJ, 972, 95
Reynolds, R. J. 1992, ApJL, 392, L35
Saldana-Lopez, A., Domìnguez, A., Pérez-González, P. G., et al. 2021, MNRAS, 507, 5144
Schiminovich, D., Friedman, P. G., Martin, C., & Morrissey, P. F. 2001, ApJL, 563, L161
Schlegel, D. J., Finkbeiner, D. P., & Davis, M. 1998, ApJ, 500, 525
Sciama, D. W. 1990, ApJ, 364, 549
Shelton, R. L., Kruk, J. W., Murphy, E. M., et al. 2001, ApJ, 560, 730
Shull, J. M., Roberts, D., Giroux, M. L., Penton, S. V., & Fardal, M. A. 1999, AJ, 118, 1450
Snowden, C. L., Cox, D. P., McCammon, D., & Sanders, W. T. 1990, ApJ, 354, 211
Spergel, D. N., Verde, L., Peiris, H. V., et al. 2003, ApJS, 148, 175
Stern, S. A. 2008, SSRv, 140, 3
Stern, S. A., Bagenal, F., Ennico, K., et al. 2015, Sci, 350, aad1815
Stern, S. A., Becker, T. M., Parker, J. W., et al. 2025, New Horizons Alice Kuiper Belt Extended Mission 2 Raw Data Collection, URN:nasa:pds:nh_alice:kem2_raw::1.0, NASA Planetary Data System, doi:10.26007/03vn-5336
Stern, S. A., Slater, D. C., Scherrer, J., et al. 2008, SSRv, 140, 155
Stern, S. A., Weaver, H. A., Spencer, J. R., et al. 2019, Sci, 364, eaaw9771
Symons, T., Zemcov, M., Cooray, A., Lisse, C., & Poppe, A. R. 2023, ApJ, 945, 45
Tennyson, P. D., Henry, R. C., Feldman, P. D., & Hartig, G. F. 1988, ApJ, 330, 435
Vallerga, J. V. 1998, ApJ, 497, 921
Weaver, H. A., Cheng, A. F., Morgan, F., et al. 2020, PASP, 132, 035003
Wenger, M., Ochsenbein, F., Egret, D., et al. 2000, A&AS, 143, 9
Witt, A. N., Friedmann, B. C., & Sasseen, T. P. 1997, ApJ, 481, 809
Witt, A. N., & Petersohn, J. K. 1994, in ASP Conf. Ser. 58, The First Symp. Infrared Cirrus and Diffuse Interstellar Clouds, ed. R. M. Cutri & W. B. Latter (San Francisco, CA: ASP), 91
Xu, C. K., Donas, J., Arnouts, S., et al. 2005, ApJL, 619, L11
Zemcov, M., Arcavi, I., Arendt, R., et al. 2018, PASP, 130, 115001
Zemcov, M., Immel, P., Nguyen, C., et al. 2017, NatCo, 8, 15003